International Journal of Rock Mechanics & Mining Sciences 137 (2021) 104543

Contents lists available at ScienceDirect

International Journal of Rock Mechanics and Mining Sciences

journal homepage: http://www.elsevier.com/locate/ijrmms

Simulating two-phase flow and geomechanical deformation in fractured karst reservoirs based on a coupled hydro-mechanical model

Lijun Liu [a,1], Zhaoqin Huang [a,1], Jun Yao [a,*], Qinghua Lei [b], Yuan Di [c], Yu-Shu Wu [d], Kai Zhang [a], Shiti Cui [e]

[a] Research Centre of Multiphase Flow in Porous Media, China University of Petroleum (East China), Qingdao, China
[b] Department of Earth Sciences, ETH Zurich, Zurich, Switzerland
[c] College of Engineering, Peking University, Beijing, China
[d] Petroleum Engineering Department, Colorado School of Mines, Golden, CO, United States
[e] Research Institute of Exploration and Development, Tarim Oilfield Company, Korla, China

ARTICLE INFO

Keywords:
Coupled hydro-mechanical model
Two-phase flow
Fractured karst systems
Cavities
Fractures

ABSTRACT

Two-phase flow in fractured and karstified porous media subject to coupled hydro-mechanical conditions is an important issue for oil recovery in carbonate reservoirs. However, due to the co-existence of porous media flow, fracture flow and free flow, as well as their couplings with geomechanical deformation, modeling the behavior of fractured karst systems remains challenging. In this work, a novel coupled hydro-mechanical model for simulating the complex behavior of fractured and karstified porous media is developed. Two-phase Darcy's equation is used to describe fluid flow in both matrix and fractures, while the free flow in cavities is considered based on an assumption of phase instantaneous gravity segregation. A modified Barton-Bandis's constitutive model is used to mimic the nonlinear fracture deformation. The cavity deformation is solved based on the fluid pressure on the cavity boundaries. A mixed finite volume-finite element method and a fixed-stress iterative splitting method are adopted to numerically solve the coupled system of equations. The model is then applied to a series of 2D and 3D problems to unravel the impacts of fractures and cavities on two-phase flow and geomechanical deformation in fractured karst systems. The results indicate that cavities hinder water breakthrough due to storage effects, while water may quickly migrate through highly conductive fractures. Cavities tend to dominate the flow and mechanical processes even though fractures are present as well. Significant stress concentration is observed around cavities. Furthermore, the results of 3D cases imply that phase gravity segregation in cavities leads to lower water saturation in the area above cavities and delays water breakthrough.

1. Introduction

Carbonate reservoirs have played an important role in providing energy for the global demand. Understanding the coupled hydro-mechanical processes involving two-phase flow in the subsurface is critical for predicting and optimizing oil recovery in carbonate reservoirs. However, different from conventional homogenous porous media, carbonate reservoirs are often characterized by multiscale porosity structures, including porous matrix, natural fractures and karstified cavities.[1,2] The co-existence of porous media flow, fracture flow and free flow as well as their couplings with the mechanical deformation in such complex systems, renders hydro-mechanical modeling of fractured karst systems very challenging.

In the past, several models have been developed to study fluid flow in fractured vuggy media, such as equivalent continuum model,[3–5] triple continuum model,[6,7] and discrete fracture-vug model.[8–10] The equivalent continuum model treats the system as a single effective medium. The upscaling approaches, such as the homogenization theory[3,4] and volume averaging method,[5] are usually used to obtain the effective anisotropic permeability tensor. The advantages of such an equivalent continuum model include the simple data requirement and high computational efficiency, but the interactions among matrix, fractures and cavities are highly simplified by using effective or equivalent parameters. It neglects numerous fine-scale details inherent in

* Corresponding author.
E-mail address: rcogfr_upc@126.com (J. Yao).
[1] The first two authors contributed equally to this paper.

https://doi.org/10.1016/j.ijrmms.2020.104543
Received 13 May 2020; Received in revised form 10 September 2020; Accepted 4 November 2020
Available online 26 November 2020
1365-1609/

high-resolution geological models, which should be used with caution when fine-scale structures have significant impacts on the overall flow behavior.[11] The triple continuum model characterizes the fractured karst media by dividing the entire domain into three superimposed and interacting subdomains (i.e. matrix, fracture, and cavity), and inter-porosity flow functions are used to couple the three subsystems.[7] However, due to the simplifications on the fracture-cavity configuration, the triple continuum model is not well suited for the modeling of a small number of larger-scale fractures and cavities, which may dominate the flow.[12] To overcome these limitations, the discrete fracture-vug model has been developed to explicitly model fractures and cavities. In this method, Darcy's law is applied for solving the flow in porous rock and fractures, while Navier-Stokes equations are used for analyzing the free flow in cavities. The Beavers-Joseph-Staffman (BJS)[13,14] interface conditions are adopted to couple the two different governing equations. Nevertheless, most of discrete fracture-vug models were focused on single-phase flow, except for a few studies that studied two-phase porous-free flow in a highly simplified system involving simple cavity geometry and no fracture.[15–21]

As the structures of weakness in fractured karst media, fractures and cavities are prone to significant deformation under in-situ stress loadings. To properly describe the fracture deformation under normal and shear stresses, a number of constitutive models have been developed.[22–29] Among these models, the empirical model proposed by Barton and Bandis[25] is widely used, which considers the peak shear strength, fracture roughness degradation, and dilation in pre-peak and post-peak stages. Asadollahi and Tonon[29] further improved the Barton-Bandis's model to better estimate the peak shear displacement and shear dilation. Such a fracture constitutive model has been implemented into several numerical methods, such as distinct element method (DEM),[30,31] finite element method (FEM),[32–36] combined finite-discrete element method (FDEM),[37,38] and extended finite element method (XFEM),[39–41] to simulate the geomechanical deformation of fractured rocks. The coupling with flow can be further implemented based on hydro-mechanical calculation. For example, zero-thickness interface elements can be easily incorporated into standard FEM programs, and integrated with the discrete fracture model (DFM) using the same grid structure[42] for flow simulation. On the other hand, several studies have been conducted to analyze the deformation of cavities. Lewandowska and Auriault[43] developed an equivalent continuum model for hydro-mechanical modeling of porous media with single fracture/cavity. The homogenization method is used to derive the equivalent parameters, such as equivalent permeability and mechanical properties. Yan et al.[44] further improved the equivalent continuum model to consider multiple fractures and cavities. However, the previously mentioned limitations of the equivalent continuum method hold for these coupled models. Recently, Zhang et al.[45] developed a numerical method to explicitly simulate the coupled hydro-mechanical behavior of both fractures and cavities. In their method, cavities were treated as virtual volumes of equal pressure in each cavity, and fractures were represented as thin layers requiring local grid refinement. Cavities were assumed incompressible during each time step, which, however, may cause numerical instability. The high computational costs associated with refined grids also limit its applicability for complex fractured karst porous media. Moreover, to accurately solve the hydromechanical coupled problem, two solution strategies, i.e. fully coupled and sequential-implicit methods, are usually adopted. The fully coupled method is known by its unconditional stability and high accuracy, but requires careful implementation with substantial local memory requirements, specialized linear solvers, and complicated code management.[39,46,52] Compared with the fully coupled method, the sequential methods have inherent advantages from the standpoint of customization, software reuse and code modularity, among which the fixed-stress split method has proven to be unconditionally stable and systematically developed by researchers.[46–53]

It can be seen that significant efforts have been made to develop appropriate models for coupled hydro-mechanical modeling of fractured karst systems. However, to our best knowledge, hydro-mechanical modeling with two-phase flow calculation has not been achieved for fractured karst reservoirs due to the extremely high computational complexity, although coupled two-phase porous-free flow (without geomechanics) in fractured vuggy media[15–19] and coupled two-phase flow and geomechanics in fractured media[54] have both been studied. Therefore, the objective of this work is to develop an efficient coupled hydro-mechanical model for studying two-phase porous-free flow and geomechanics in fractured karst systems. Two-phase Darcy's equation is solved to model fluid flow in both porous matrix and fracture networks, while the free flow in cavities is calculated based on phase instantaneous gravity segregation. The deformation of porous matrix is governed by the classical Biot's poroelasticity theory. The modified Barton-Bandis's model is used to describe the normal closure, shear deformation and shear-induced dilation of natural fractures. The fluid pressure is applied on the cavity boundaries when computing the deformation of cavities. Finally, a mixed finite volume method-finite element method (FVM-FEM) is adopted for space discretization and deriving numerical schemes: FVM together with DFM is used for solving flow, while FEM with zero-thickness interface elements is applied for calculating geomechanics. The coupled problem is then iteratively solved by the fixed-stress split method.

The rest of the paper is organized as follows: in section 2, the mathematical model for coupled two-phase flow and geomechanics in fractured karst porous media is presented; in section 3, detailed numerical schemes and solution methods are formulated; in section 4, a validation of the proposed model is presented; in section 5, the model is applied to study a series of 2D and 3D problems; finally, a few conclusions are drawn.

2. Mathematical model

In this section, the mathematical models that describe the two-phase flow and mechanical behaviors of fractured karst porous media are presented.

2.1. Flow governing equations

An isothermal water-oil two-phase system in fractured vuggy porous media is considered. The fluid flow in porous matrix and fractures obeys Darcy's law. Conditions of equal pressure and two-phase instantaneous gravity segregation are assumed for free flow in cavities (to be described in detail in section 3.2). The mass balance equation in matrix, fracture, and cavity domains is written as

$$\frac{\partial}{\partial t}(\varphi\rho_\beta S_\beta) = -\nabla\cdot(\rho_\beta \mathbf{v}_\beta) + q_\beta, \tag{1}$$

where the subscript $\beta = \mathrm{o}$ or w denotes the fluid phase, i.e. oil or water, respectively; φ is the reservoir porosity, defined as the ratio of pore volume in deformable configuration to the total volume of the undeformed configuration; ρ is the phase density; S is the saturation; q is the sink/source term; $\boldsymbol{v}$ is the phase velocity in matrix or fractures, determined by Darcy's law

$$\mathbf{v}_\beta = -\frac{kk_{\mathrm{r}\beta}}{\mu_\beta}\nabla\psi_\beta, \tag{2}$$

where k is the permeability; k_r is the relative permeability; μ is the dynamic viscosity; $\psi = p - \rho gD$ is the phase potential; p is the phase pressure; D is the depth.

Besides, the following constraint equations are required

$$S_o + S_w = 1, \tag{3}$$

$$p_\mathrm{w} = p_\mathrm{o} - p_\mathrm{cow}, \tag{4}$$

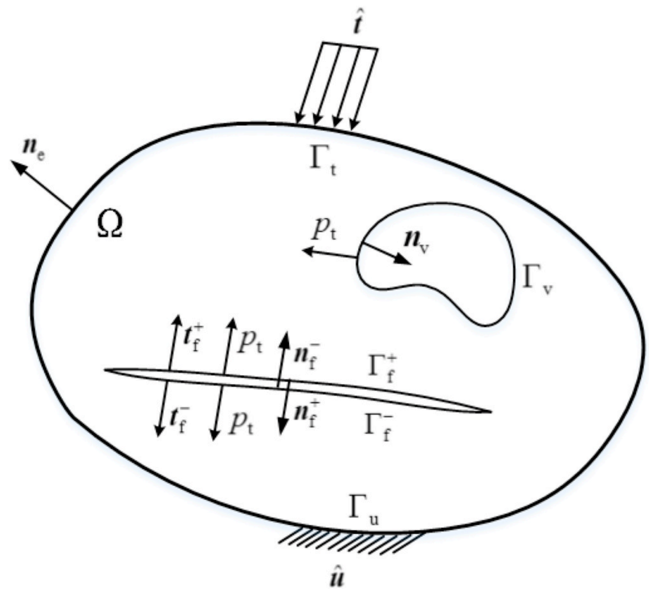

Fig. 1. Schematic of fractured karst porous media. The entire domain contains three types of media: porous matrix, fractures, and cavities.

where p_{cow} is the oil/gas capillary pressure in matrix. The capillary pressure is modified with porosity and permeability according to the Leverett function[55]:

$$p_{cow} = p_{cow,0}\sqrt{\frac{k_{m0}\varphi_m}{k_m\varphi_{m0}}}, \tag{5}$$

where the subscript m denotes matrix, and 0 represents the initial state. The capillary pressure in fractures and cavities is omitted.

2.2. Geomechanical governing equations

The quasi-static momentum equilibrium equation in the solid domain is expressed as

$$\nabla\cdot\boldsymbol{\sigma} + \mathbf{b} = 0, \tag{6}$$

where $\boldsymbol{b}$ is the body force vector; following a convention with tension being positive, the total stress tensor $\boldsymbol{\sigma}$ is defined as[56]

$$\boldsymbol{\sigma} = \boldsymbol{\sigma}' - \alpha p_t \mathrm{I}, \tag{7}$$

where $\boldsymbol{\sigma}' = \boldsymbol{C} : \boldsymbol{\varepsilon}$ is the effective stress tensor; $\boldsymbol{C}$ and α are the elasticity tensor and Biot coefficient, respectively; $p_t = \Sigma p_\beta S_\beta$ is the total pressure; $\mathbf{I}$ is the identity tensor; assuming the deformation to be infinitesimal, the strain tensor $\boldsymbol{\varepsilon}$ can be calculated as

$$\boldsymbol{\varepsilon} = \frac{1}{2}\left(\nabla\boldsymbol{u} + \nabla^{\mathrm{T}}\boldsymbol{u}\right), \tag{8}$$

where ∇ indicates the gradient operator, and the superscript T indicates the transpose operator.

The geomechanical boundary conditions of fractured karst systems are schematically shown in Fig. 1. The solid domain Ω is subjected to a prescribed displacement $\hat{\mathbf{u}}$ on its Dirichlet boundary Γ_u, a prescribed traction $\hat{\mathbf{t}}$ on its Neumann boundary Γ_t, fluid pressure on the cavity boundary Γ_v, and fluid pressure and traction along the fracture boundary $\Gamma_f^{\pm}$ as follows

$$\begin{aligned} \mathbf{u} &= \hat{\mathbf{u}} \ \ on\ \Gamma_u \\ \boldsymbol{\sigma}\cdot\mathbf{n}_e &= \hat{\mathbf{t}} \ \ on\ \Gamma_t \\ \boldsymbol{\sigma}\cdot\mathbf{n}_v &= -p_t\mathrm{I}\cdot\mathbf{n}_v \ \ on\ \Gamma_v \\ \boldsymbol{\sigma}\cdot\mathbf{n}_f^+ &= -p_t\mathrm{I}\cdot\mathbf{n}_f^+ - \mathbf{t}_f^+ \ \ on\ \Gamma_f^+ \\ \boldsymbol{\sigma}\cdot\mathbf{n}_f^- &= -p_t\mathrm{I}\cdot\mathbf{n}_f^- - \mathbf{t}_f^- \ \ on\ \Gamma_f^- \end{aligned} \tag{9}$$

where $\boldsymbol{n}_e$ is the unit outward normal vector on outer boundary; $\boldsymbol{n}_v$ is the unit normal vector on the cavity boundary; $\mathbf{n}_f^+$ and $\mathbf{n}_f^-$ are unit normal vectors on the positive and negative fracture boundary with $\mathbf{n}_f^+ = -\mathbf{n}_f^-$; $\mathbf{t}_f^+$ and $\mathbf{t}_f^-$ are the tractions acting on the fracture boundary with $\mathbf{t}_f^+ = -\mathbf{t}_f^-$, which is a function of the fracture closure vector $\boldsymbol{\zeta}$. Notice that the Biot coefficient of fractures is set as 1.0 by default, while the fluid pressure is directly applied on the cavity boundaries without the scaling of Biot coefficient.[57]

2.3. Constitutive relationships

A series of constitutive relationships are adopted to couple the flow properties of matrix, fractures and cavities with the geomechanical responses (i.e. stress and strain). For matrix, the porosity variation in a deformable porous medium can be expressed as[58]

$$\Delta\varphi_m^* = \frac{(\alpha_m - \varphi_m^*)}{K_m}(\Delta p_t + \Delta\sigma_v), \tag{10}$$

where K is the drained bulk modulus; σ_v is the total mean stress; φ^* is the true porosity, defined as the ratio of the pore volume in the deformed configuration to the total volume of the deformed configuration[52,58]; the relation between the true porosity φ^* and the reservoir porosity φ is given as $\varphi = \varphi^*(1+\varepsilon_v)$; ε_v is the volumetric strain. Then, the matrix permeability can be calculated based on the Kozeny-Carman model[59] as follows

$$k_m = k_{m0}\left(\frac{\varphi_m}{\varphi_{m0}}\right)^3\left(\frac{1-\varphi_{m0}}{1-\varphi_m}\right)^2. \tag{11}$$

The Kozeny-Carman model is used here because of its good theoretical basis and justified applicability for carbonates.[60] Other porosity-permeability relations, such as the power-law correlation presented in Davies and Davies[61] and Rutqvist et al.,[53] can be also equally applied.

For natural fractures, the Barton-Bandis's model[23,24] is used to relate the fracture normal closure ζ_n with the normal effective compressive stress σ_n acting on the fracture surfaces

$$\sigma_n = \frac{\kappa_{ni}\zeta_n}{1-\zeta_n/\zeta_m}, \tag{12}$$

where κ_{ni} is the initial normal stiffness; ζ_m is the allowed maximum closure. κ_{ni} and ζ_m may be estimated by[23]

$$\kappa_{ni} = -7.15 + 1.75\mathrm{JRC} + 0.02\frac{\mathrm{JCS}}{w_0}, \tag{13}$$

$$\zeta_m = -0.1032 - 0.0074\mathrm{JRC} + 1.1350\left(\frac{\mathrm{JCS}}{w_0}\right)^{-0.2510}. \tag{14}$$

where JRC is the joint roughness coefficient; JCS is the joint compressive strength (in the unit of MPa); w_0 is the initial aperture. JRC and JCS can be determined from experimental measurements, such as laboratory tilt tests or shear box experiments,[62] on joint samples coring from reservoirs, and the values under a third loading cycle can be adopted since in-situ fractures are considered to behave in a manner similar to the third or fourth cycle.[63] Then, the normal fracture stiffness κ_{nn} is derived as

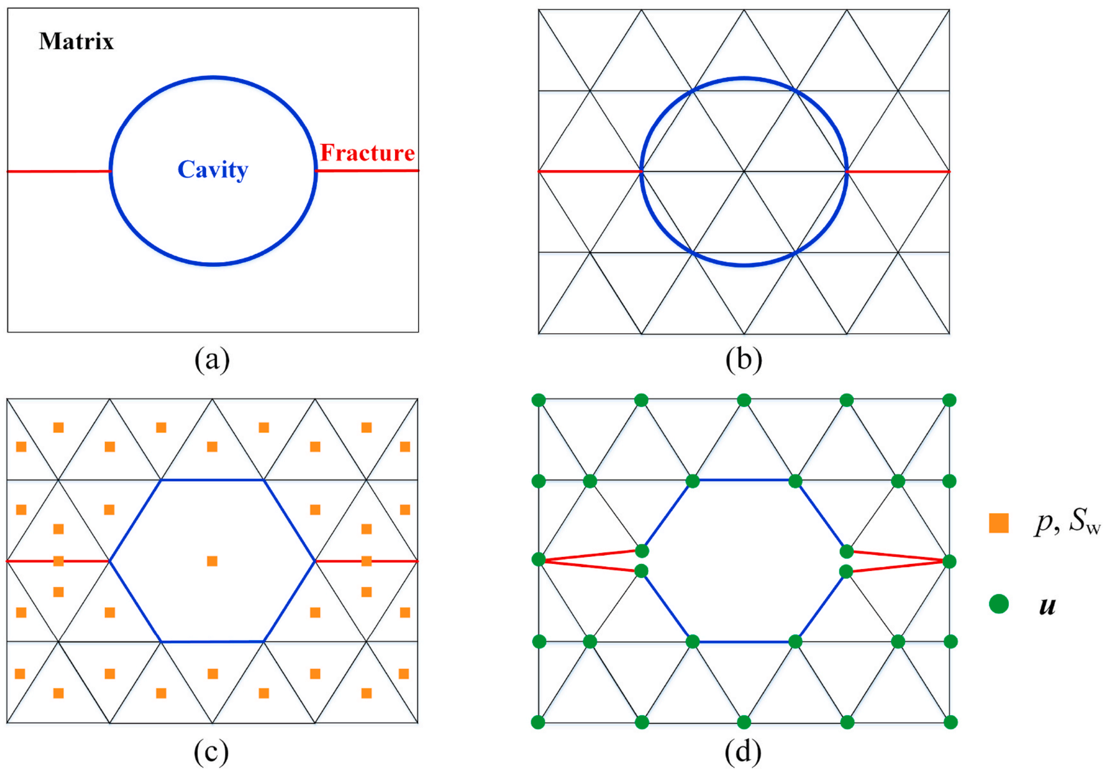

Fig. 2. Schematic of (a) geological model, (b) unstructured geometrical grids, (c) grid structure for flow, and (d) grid structure for geomechanics.

$$\kappa_{nn} = \frac{\partial \sigma_n}{\partial \zeta_n} = \frac{(\sigma_n + \kappa_{ni}\zeta_m)^2}{\kappa_{ni}\zeta_m^2}. \tag{15}$$

The shear behavior of fractures is described by an empirical model proposed by Barton and Choubey[62]

$$\tau_t = \sigma_n \tan\left[\mathrm{JRC}_{mob} \log\left(\frac{\mathrm{JCS}}{\sigma_n}\right) + \phi_{mob}\right], \tag{16}$$

where τ_t is the shear stress (MPa); JRC_{mob} is the mobilized joint roughness coefficient; ϕ_{mob} is the mobilized friction angle. The calculation of JRC_{mob} and ϕ_{mob} refers to Asadollahi et al.[28] Then the shear fracture stiffness κ_{tt} is derived as follows

$$\kappa_{tt} = \frac{\partial \tau_t}{\partial \zeta_t} = \sigma_n \cdot \left[\frac{\partial \mathrm{JRC}_{mob}}{\partial \zeta_t} \log\left(\frac{\mathrm{JCS}}{\sigma_n}\right) + \frac{\partial \phi_{mob}}{\partial \zeta_t}\right] \cdot \cos^{-2}\left[\mathrm{JRC}_{mob} \log\left(\frac{\mathrm{JCS}}{\sigma_n}\right) + \phi_{mob}\right], \tag{17}$$

where ζ_t is the tangential separation of the opposite fracture planes.

Furthermore, shear dilation may occur during the shearing process. The shear-induced dilation ζ_v can be calculated by[28]

$$\zeta_v = \begin{cases} \dfrac{\zeta_{peak}}{3} \tan\left[\mathrm{JRC} \cdot \log\left(\dfrac{\mathrm{JCS}}{\sigma_n}\right)\right]\left(\dfrac{\zeta_t}{\zeta_{peak}}\right)\left(\dfrac{2\zeta_t}{\zeta_{peak}} - 1\right), & \zeta_t \le \zeta_{peak} \\ \displaystyle\int_{\zeta_{peak}}^{\zeta_t} \tan\left[\mathrm{JRC} \cdot \log\left(\frac{\mathrm{JCS}}{\sigma_n}\right)\left(\frac{\zeta_{peak}}{\xi}\right)^{0.381}\right] d\xi + \zeta_{v,\,peak}, & \zeta_t > \zeta_{peak} \end{cases}, \tag{18}$$

where ζ_{peak} is the peak shear displacement, and $\zeta_{v,peak}$ is the dilation corresponding to ζ_{peak}.

The fracture mechanical aperture w_m can be calculated after obtaining the fracture closure ζ_n and shear dilation ζ_v

$$w_m = w_0 - \zeta_n + \zeta_v. \tag{19}$$

To further derive the hydraulic aperture defined as the equivalent aperture for laminar flow, the empirical relation proposed by Olsson and Barton[64] is used to relate the hydraulic aperture w_h with the mechanical aperture w_m as

$$w_h = \begin{cases} w_m^2/\mathrm{JRC}^{2.5}, & \zeta_t/\zeta_{peak} \le 0.75 \\ \sqrt{w_m}\mathrm{JRC}_{mob}, & \zeta_t/\zeta_{peak} \ge 1.0 \end{cases}, \tag{20}$$

where w_h and w_m are in the unit of μm, and the hydraulic aperture is determined by linear interpolation when $0.75 < \zeta_t/\zeta_{peak} < 1.0$.

Based on the hydraulic aperture, the fracture porosity φ_f can be updated, and the permeability k_f can be calculated according to the cubic law[65]

$$\varphi_f = \frac{w_h}{w_{h0}} \varphi_{f0}, \tag{21}$$

$$k_f = \frac{w_h^2}{12}. \tag{22}$$

For cavities, the constitutive model refers to the relation between cavity volume and the effective stress acting on the cavity boundary. However, the relation is difficult to be analytically obtained because cavity deformation is affected by various factors, such as cavity geometry, stress distribution, and matrix properties. In this paper, a cavity-volume-updating method modified from Zhang et al.[45] is adopted, which will be discussed in more detail in section 3.3.

3. Numerical schemes

In this section, we present the numerical formulations. With the grid structure defined, the FVM and FEM are used for the space discretization of the governing equations for flow and geomechanics, respectively. The coupled system of equations is iteratively solved by the fixed-stress splitting method. The simulation code is programmed using Fortran 90, while Gmsh[66] and Tecplot[67] are used for preprocessing and post-processing, respectively.

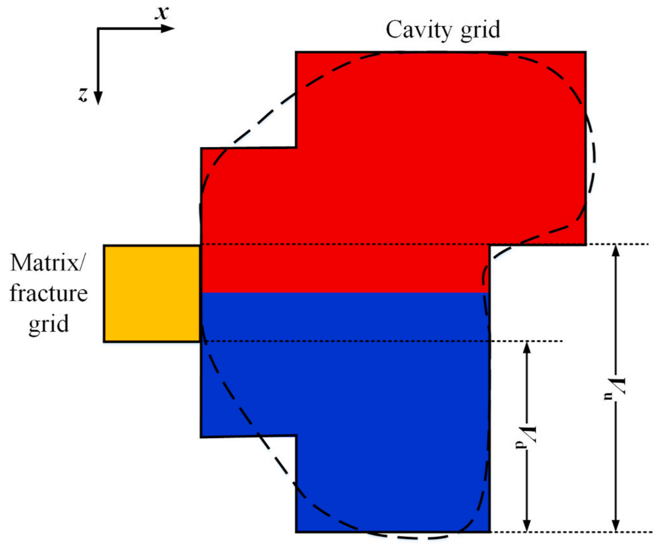

Fig. 3. Schematic of a vertical slice of a cavity grid and one of its connected matrix/fracture grids. The irregular cavity (dashed line) is represented by a straight-edged structure (cavity grid). The red and blue parts represent the oil and water phases, respectively. (For interpretation of the references to colour in this figure legend, the reader is referred to the Web version of this article.)

3.1. Space discretization

The problem domain, as shown in Fig. 2a, is initially discretized using a conformed grid. As shown in Fig. 2b, triangular elements are used to discretize the matrix and cavity domains, while linear elements are used for the discretization of pre-existing fractures. Based on the geometrical grids, the specific space discretization for flow and geomechanics problems are illustrated. For flow, the cavity grid is firstly formed by merging all the grids in the cavity region. Then, a control volume is associated to each grid with primary variables, i.e. pressure and saturation, locating at the grid center (orange point) as shown in Fig. 2c. For geomechanics, the zero-thickness interface elements are applied to represent the discontinuity condition along fractures by splitting the fracture nodes, and the displacement unknowns are located at the grid vertices (green point) as shown in Fig. 2d. Following a similar procedure, a 3D grid system can also be established.

3.2. Discretized flow equations

The flow equation (1) is discretized in space in the context of the FVM, and the time derivative is approximated using a backward, first-order finite-difference scheme. The discretized equation can be written in residual form as

$$R_{\beta,i}^{n+1} = \left[(\varphi\rho_\beta S_\beta)_i^{n+1} - (\varphi\rho_\beta S_\beta)_i^n\right]\frac{V_i}{\Delta t} - \sum_{j\in\eta_i}\left[(\rho_\beta\lambda_\beta)_{ij+1/2}^{n+1} T_{ij}^{n+1}\left(\psi_{\beta,j}^{n+1} - \psi_{\beta,i}^{n+1}\right)\right] - V_i q_{\beta,i}^{n+1}, \tag{23}$$

where the subscript i denotes the index of grid block; the superscripts n and $n+1$ represent the previous and current times, respectively; η_i represents all the neighbors of the grid block i; the subscript $ij+1/2$ denotes an upstream weighting quantity at the interface of the grid blocks i and j; V is the grid volume; Δt is the current time step size; λ_β is the mobility of the fluid phase β, defined as $\lambda_\beta = k_{r\beta}/\mu_\beta$; T_{ij} is the transmissivity associated with the connection between the grid blocks i and j, which can be divided into three categories: transmissivity between matrix grids, fracture-related transmissivity, and cavity-related transmissivity.

The transmissivity between matrix grids can be evaluated by two-point flux approximation (TPFA) as follows[68]

$$T_{ij} = \frac{T_i T_j}{T_i + T_j}, \tag{24}$$

where T_i is the one-sided transmissivity associated with the matrix block i, defined as

$$T_i = \frac{k_i A_{ij}}{d_i}\mathbf{n}_i\cdot\mathbf{c}_i, \tag{25}$$

where k_i is the absolute permeability of the block i; A_{ij} is the interface area between the grid blocks i and j; d_i is the distance between the centroid of the block i and the centroid of the interface; $\boldsymbol{n}_i$ is the unit normal to the interface inside the block i; $\boldsymbol{c}_i$ is the unit vector along the direction of the line joining the centroid of the block i to the centroid of the interface. Notice that TPFA may lead to inconsistent fluxes on general meshes and for anisotropic permeability tensors. In that case, the multi-point flux approximation method (MPFA) can be used for higher numerical accuracy.[69]

The fracture-related transmissivity includes the transmissivity between matrix and fracture grids and transmissivity between fracture grids. For the transmissivity between matrix/fracture grids, as well as

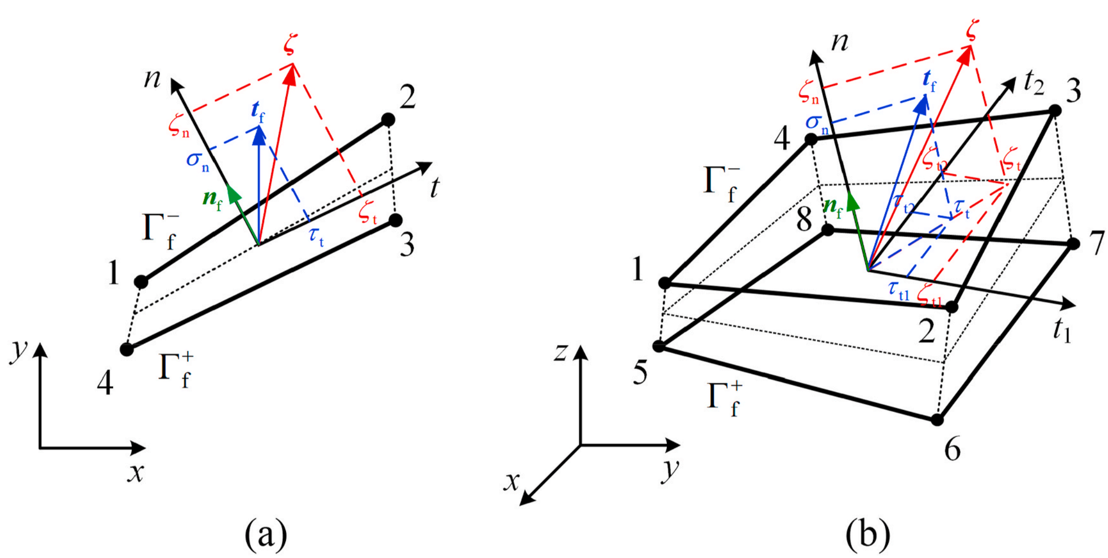

Fig. 4. Schematic of fracture deformation related variables ($\boldsymbol{\zeta}$, $\boldsymbol{t}_f$, and $\boldsymbol{n}_f$) in the (a) 2D and (b) 3D local coordinates.

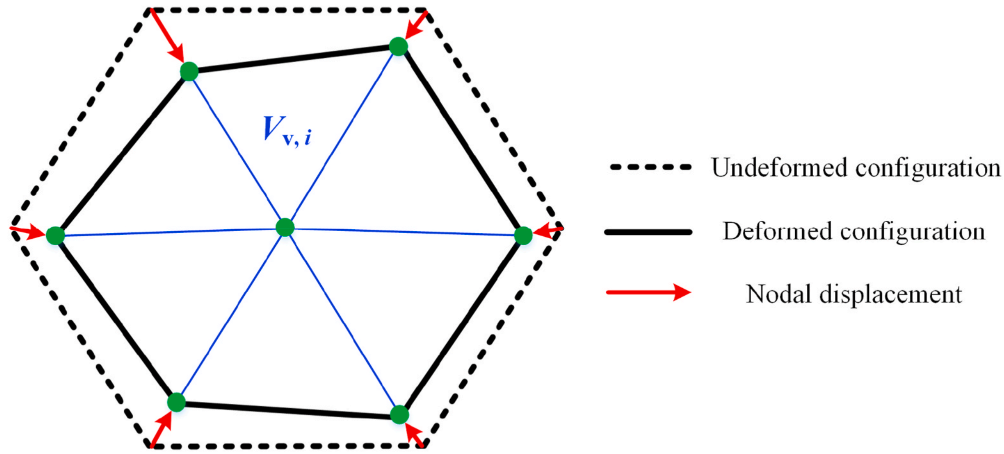

Fig. 5. Schematic showing the cavity volume variation. The deformed cavity is decomposed into a series of triangular elements, and the cavity volume is updated by summing up the volumes of these elements.

fracture grids in one individual fracture, equation (24) is still applicable. While for the fracture grids at fracture intersections, which involve multiple fracture grids (commonly more than two grids), the approximation, i.e. star-delta transformation, proposed by Karimi-Fard et al.[70] is used

$$T_{ij} = \frac{T_i T_j}{\sum_{k=1}^{n_f} T_k}, \tag{26}$$

where n_{f} is the number of intersected fracture grids.

The cavity-related transmissivity consists of the matrix/cavity transmissivity and fracture/cavity transmissivity. Because of the extremely high conductivity of cavities, the cavity-related transmissivity may be approximated by the one-sided transmissivity of the matrix or fracture grid, as calculated from equation (25).

In addition, the water-oil two phase is assumed to be separated vertically in cavities with water locating in the lower space and oil occupying the upper space. Based on this assumption, the phase mobility λ_β is redefined as follows

$$\lambda_\beta = \tilde{k}_{\mathrm{r}\beta} \Big/ \mu_\beta, \tag{27}$$

where the viscosity μ and relative permeability $\tilde{k}_{\mathrm{r}}$ are still determined by upstream weighting method, but $\tilde{k}_{\mathrm{r}}$ is redefined. When fluid flows from matrix or fractures into cavities, $\tilde{k}_{\mathrm{r}}$ takes the relative permeability of matrix or fractures. Reversely, $\tilde{k}_{\mathrm{r}}$ takes the phase flow fraction, which, for 2D scenarios, can be assigned as the saturation in cavities as

$$\tilde{k}_{\mathrm{r}\beta} = S_\beta. \tag{28}$$

For 3D scenarios, $\tilde{k}_{\mathrm{r}}$ is derived as follows for a structured hexahedral grid system. Fig. 3 shows a vertical slice of a cavity grid and one of its connected grids, in which the irregular cavity is represented by a straight-edged structure obtained by merging the grids in the cavity region. The phase flow fraction $\tilde{k}_{\mathrm{r}}$ can be expressed as

$$\tilde{k}_{\mathrm{rw}} = \begin{cases} 0, & S_{\mathrm{w}} \le S_{\mathrm{d}} \\ \dfrac{S_{\mathrm{w}} - S_{\mathrm{d}}}{S_{\mathrm{u}} - S_{\mathrm{d}}}, & S_{\mathrm{d}} < S_{\mathrm{w}} \le S_{\mathrm{u}}\,, \\ 1, & S_{\mathrm{u}} < S_{\mathrm{w}} \end{cases} \quad \tilde{k}_{\mathrm{ro}} = 1 - \tilde{k}_{\mathrm{rw}}, \tag{29}$$

where S_{u} and S_{d} are the saturations corresponding to the upper and lower bounds of the connected grid, calculated by

$$S_{\mathrm{u}} = \frac{V_{\mathrm{u}}}{V_{\mathrm{v}}} \qquad S_{\mathrm{d}} = \frac{V_{\mathrm{d}}}{V_{\mathrm{v}}} \tag{30}$$

where V_{v} is the cavity volume; V_{u} and V_{d} are volumes corresponding to S_{u} and S_{d}, as illustrated in Fig. 3. Clearly, V_{u} and V_{d} are commonly different for each cavity-connected grid in 3D, which need to be pre-processed. In a similar way, $\tilde{k}_{\mathrm{r}}$ can be also derived on other types of 3D grids.

Then equation (23) is solved using the Newton-Raphson iteration method, and the primary variables are updated during each iteration as follows

$$\sum_{\gamma} \frac{\partial R_{\beta,i}^{n+1}(x_{\gamma,k})}{\partial x_\gamma} \Delta x_{\gamma,k+1} = -R_{\beta,i}^{n+1}(x_{\gamma,k}) \qquad x_{\gamma,k+1} = x_{\gamma,k} + \Delta x_{\gamma,k+1} \tag{31}$$

where γ denotes the index of the primary variable; k is the Newton iteration level; x represent the primary variables, such as oil pressure p_{o} and water saturation S_{w}. The Newton-Raphson iteration continues, and the primary variables are updated until the residuals are less than the tolerance for convergence.

3.3. Discretized geomechanical equations

The geomechanical equation is discretized by the FEM method. With the virtual work theory and divergence theorem, the weak form for equations (6) and (7) can be derived as

$$\int_\Omega \delta\boldsymbol{\varepsilon} : \boldsymbol{\sigma}' \, \mathrm{d}\Omega - \int_\Omega \delta\boldsymbol{\varepsilon} : \alpha p_t \mathrm{I} \, \mathrm{d}\Omega - \int_\Omega \delta\boldsymbol{u} \cdot \mathbf{b} \mathrm{d}\Omega + \int_{\Gamma_{\mathrm{f}}} \delta\boldsymbol{\zeta} \cdot \mathbf{t}_{\mathrm{f}} \, \mathrm{d}\Gamma + \int_{\Gamma_{\mathrm{f}}} \delta\boldsymbol{\zeta} \cdot p_t \mathrm{I} \cdot \mathbf{n}_{\mathrm{f}} \, \mathrm{d}\Gamma + \int_{\Gamma_{\mathrm{v}}} \delta\boldsymbol{u} \cdot p_t \mathrm{I} \cdot \mathbf{n}_{\mathrm{v}} \, \mathrm{d}\Gamma - \int_{\Gamma_t} \delta\boldsymbol{u} \cdot \widehat{\mathbf{t}} \, \mathrm{d}\Gamma = 0 \tag{32}$$

where $\mathbf{n}_{\mathrm{f}} = \mathbf{n}_{\mathrm{f}}^{+} = -\mathbf{n}_{\mathrm{f}}^{-}$, and $\mathbf{t}_{\mathrm{f}} = \mathbf{t}_{\mathrm{f}}^{+} = -\mathbf{t}_{\mathrm{f}}^{-}$; the displacement unknowns $\boldsymbol{u}$ are approximated by interpolating the nodal displacement $\bar{\mathbf{u}}$ with the shape functions

$$\mathbf{u} = \mathbf{N}\bar{\mathbf{u}}, \tag{33}$$

where $\boldsymbol{N}$ is the shape function matrix. $\boldsymbol{\zeta} = \boldsymbol{u}|_{\Gamma_{\mathrm{f}}^{+}} - \boldsymbol{u}|_{\Gamma_{\mathrm{f}}^{-}}$ denotes the fracture closure vector. For convenience, the fracture-related integrations, i.e. fourth and fifth terms in equation (32), are evaluated in the local coordinate system. The variables $\boldsymbol{\zeta}$, $\mathbf{t}_{\mathrm{f}}$, and $\boldsymbol{n}_{\mathrm{f}}$ are transformed into the

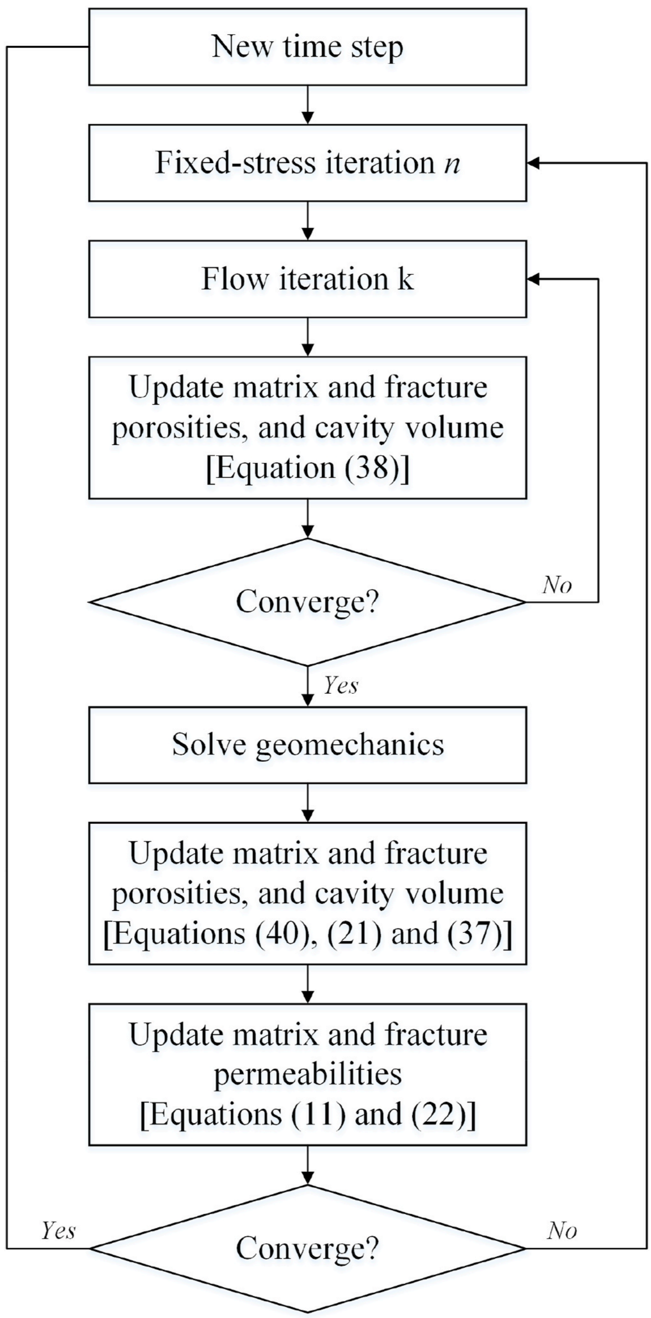

Fig. 6. Flowchart of fixed-stress iterative split method for solving coupled flow and geomechanics problem.

local coordinate system as shown in Fig. 4, but the same notations are still used in the following equations.

The local fracture closure $\boldsymbol{\zeta}$ can be approximated as

$$\boldsymbol{\zeta} = \mathbf{B}_{\rm f}\tilde{\mathbf{u}}, \tag{34}$$

where $\tilde{\mathbf{u}}$ is the nodal displacement vector of the fracture interface element; $\boldsymbol{B}_{\rm f}$ is the global displacement-closure relation matrix. Detailed formulation of $\boldsymbol{B}_{\rm f}$ can be found in Park and Paulino[71] and Ghosh et al.[72] Then the tractions acting on the fracture surface ($\sigma_{\rm n}$, $\tau_{\rm t}$) and fracture stiffness ($\kappa_{\rm nn}$, $\kappa_{\rm tt}$) can be calculated based on equations (12) and (15)–(17).

The discretized equations can be obtained by introducing the approximations, i.e. equations (33) and (34), into the weak form in equation (32), and the residual form can be expressed as

$$\mathbf{R} = \mathbf{f}_{\rm in} - \mathbf{Q} - \mathbf{f}_{\rm b} + \mathbf{f}_{\rm f} + \mathbf{Q}_{\rm f} + \mathbf{Q}_{\rm v} - \mathbf{f}_{\rm e}, \tag{35}$$

in which

$$\mathbf{f}_{\rm in} = \int_{\Omega}\mathbf{B}^{\rm T}\boldsymbol{\sigma}' d\Omega,\ \ \mathbf{Q} = \int_{\Omega}\alpha\mathbf{B}^{\rm T}\mathbf{m}\, d\Omega\, p_{\rm t},\ \ \mathbf{f}_{\rm b} = \int_{\Omega}\mathbf{N}^{\rm T}\mathbf{b}d\Omega,\ \ \mathbf{f}_{\rm f} = \int_{\Gamma_{\rm f}}\mathbf{B}_{\rm f}^{\rm T}\mathbf{t}_{\rm f}d\Gamma,$$
$$\mathbf{Q}_{\rm f} = \int_{\Gamma_{\rm f}}\mathbf{B}_{\rm f}^{\rm T}\mathbf{n}_{\rm f}d\Gamma p_{\rm t},\ \ \mathbf{Q}_{\rm v} = \int_{\Gamma_{\rm v}}\mathbf{N}^{\rm T}\mathbf{n}_{\rm v}d\Gamma p_{\rm t},\ \ \mathbf{f}_{\rm e} = \int_{\Gamma_{\rm t}}\mathbf{N}^{\rm T}\hat{\mathbf{t}}d\Gamma,$$

where $\boldsymbol{B} = \boldsymbol{LN}$, and $\boldsymbol{L}$ denotes the differential operator matrix; $\mathbf{m}$ is the vector of delta Dirac function defined as $\mathbf{m} = [1,\ 1,\ 0]^{\rm T}$ for two dimensional problems, and $\mathbf{m} = [1, 1, 1, 0, 0, 0]^{\rm T}$ for three dimensional problems. Then the nonlinear equation (35) can be solved using Newton-Raphson iteration method as follows

$$\frac{\partial\mathbf{R}\left(\overline{\mathbf{u}}_k\right)}{\partial\overline{\mathbf{u}}}\delta\overline{\mathbf{u}}_{k+1} = -\mathbf{R}\left(\overline{\mathbf{u}}_k\right) \tag{36}$$
$$\overline{\mathbf{u}}_{k+1} = \overline{\mathbf{u}}_k + \delta\overline{\mathbf{u}}_{k+1}$$

in which

$$\frac{\partial\mathbf{R}\left(\overline{\mathbf{u}}_k\right)}{\partial\overline{\mathbf{u}}} = \frac{\partial\mathbf{f}_{\rm in}^k}{\partial\overline{\mathbf{u}}} + \frac{\partial\mathbf{f}_{\rm f}^k}{\partial\overline{\mathbf{u}}} = \mathbf{K}_{\rm b} + \mathbf{K}_{\rm f},\ \ \mathbf{K}_{\rm b} = \int_{\Omega}\mathbf{B}^{\rm T}\mathbf{D}\mathbf{B}d\Omega,\ \ \mathbf{K}_{\rm f} = \int_{\Gamma_{\rm f}}\mathbf{B}_{\rm f}^{\rm T}\mathbf{D}_{\rm f}\mathbf{B}_{\rm f}d\Gamma,$$

where $\boldsymbol{D}$ is the elastic modulus matrix; $\mathbf{D}_{\rm f} = \left.\frac{\partial\mathbf{t}_{\rm f}}{\partial\boldsymbol{\zeta}}\right|_{\boldsymbol{\zeta}^k}$ is the local fracture constitutive matrix, defined as

$$\mathbf{D}_{\rm f} = \begin{bmatrix}\kappa_{\rm tt} & 0\\ 0 & \kappa_{\rm nn}\end{bmatrix}$$

in two dimensions, and

$$\mathbf{D}_{\rm f} = \begin{bmatrix}\kappa_{\rm tt}\zeta_{\rm t1}^2/\zeta_{\rm t}^2 + \tau_{\rm t}\zeta_{\rm t2}^2/\zeta_{\rm t}^3 & \kappa_{\rm tt}\zeta_{\rm t1}\zeta_{\rm t2}/\zeta_{\rm t}^2 - \tau_{\rm t}\zeta_{\rm t1}\zeta_{\rm t2}/\zeta_{\rm t}^3 & 0\\ \kappa_{\rm tt}\zeta_{\rm t1}\zeta_{\rm t2}/\zeta_{\rm t}^2 - \tau_{\rm t}\zeta_{\rm t1}\zeta_{\rm t2}/\zeta_{\rm t}^3 & \kappa_{\rm tt}\zeta_{\rm t2}^2/\zeta_{\rm t}^2 + \tau_{\rm t}\zeta_{\rm t1}^2/\zeta_{\rm t}^3 & 0\\ 0 & 0 & \kappa_{\rm nn}\end{bmatrix}$$

for three dimensional problems.

Once the geomechanical problem is solved, the cavity volume can be accordingly updated. As shown in Fig. 5, taking a 2D case as an example, the deformed cavity is decomposed into a series of triangular elements with each element composed by two nodes on the cavity boundary and the cavity center. The cavity volume $V_{\rm v}$ can be calculated by

$$V_{\rm v} = \sum_{i=1}^{n_{\rm v}} V_{{\rm v},i}, \tag{37}$$

where $n_{\rm v}$ is the number of triangular elements composing the cavity grid; $V_{{\rm v},i}$ is the volume of the i-th triangular element. Then the cavity volume can be updated with the volume of each triangular element updating according to the nodal displacement of the cavity boundary.

3.4. Solution strategy

As illustrated in Fig. 6, the fixed-stress split iterative method[46–53] is used to sequentially solve the coupled two-phase flow and geomechanics problem. In each time step, the flow problem is firstly solved with the total mean stress fixed. The matrix and fracture porosities, as well as cavity volumes, are updated during each flow iteration as follows

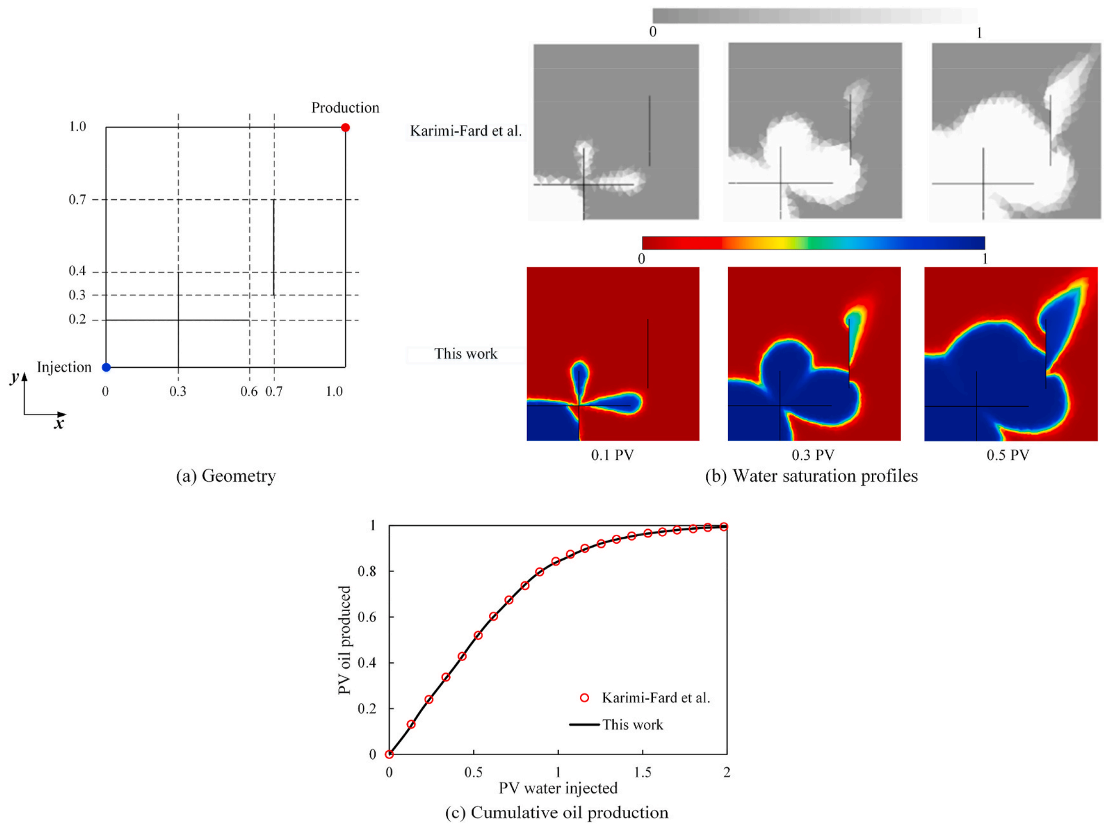

Fig. 7. (a) Geometrical configuration of the fractured medium, (b) water saturation profiles at different pore-volume (PV) water injection, and (c) cumulative oil production results obtained from Karimi-Fard et al.[70] and this work.

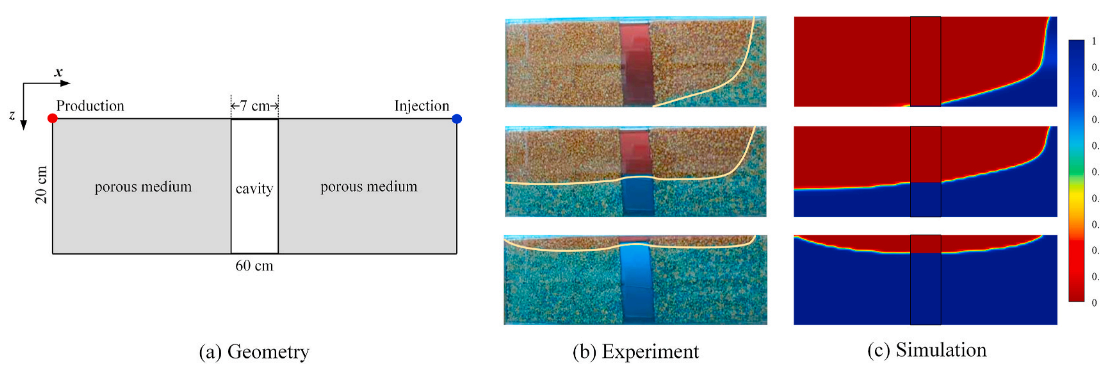

Fig. 8. (a) Geometrical representation of the experiment model (the thickness of the model is 2 cm), and water saturation profiles obtained from (b) experiment in Di et al.[73] and (c) our proposed cavity model at 20s, 80s, and 180s of water injection (from upper to lower panel).

$$\begin{aligned}
\varphi_{\mathrm{m}}^{k} &= \varphi_{\mathrm{m}}^{k-1} + \frac{\alpha(1+\varepsilon_{\mathrm{v}}) - \varphi_{\mathrm{m}}^{k-1}}{K_{\mathrm{m}}}\left(p_{\mathrm{t}}^{k} - p_{\mathrm{t}}^{k-1}\right) \\
\varphi_{\mathrm{f}}^{k} &= \varphi_{\mathrm{f}}^{k-1} + \frac{\alpha\varphi_{\mathrm{f}0}}{w_0 k_{\mathrm{nn}}}\left(p_{\mathrm{t}}^{k} - p_{\mathrm{t}}^{k-1}\right) \\
V_{\mathrm{v}}^{k} &= V_{\mathrm{v}}^{k-1} + \left.\frac{\partial V_{\mathrm{v}}}{\partial p}\right|_{\boldsymbol{\sigma}^n}\left(p_{\mathrm{t}}^{k} - p_{\mathrm{t}}^{k-1}\right)
\end{aligned} \tag{38}$$

where $\partial V_{\mathrm{v}}/\partial p$ can be numerically calculated as

$$\left.\frac{\partial V_{\mathrm{v}}}{\partial p}\right|_{\boldsymbol{\sigma}^n} = \frac{V_{\mathrm{v}}(p^k+\delta p)|_{\boldsymbol{\sigma}^n} - V_{\mathrm{v}}(p^k)|_{\boldsymbol{\sigma}^n}}{\delta p}. \tag{39}$$

Then the geomechanical problem is solved with the updated bulk pressure obtained from the flow problem. The matrix porosity is updated as follows

$$\varphi_{\mathrm{m}} = \varphi_{\mathrm{m}0} + \alpha(\varepsilon_{\mathrm{v}} - \varepsilon_{\mathrm{v}0}) + \frac{(\alpha-\varphi_{\mathrm{m}0})(1-\alpha)}{K_{\mathrm{m}}}(p_{\mathrm{t}} - p_{\mathrm{t}0}). \tag{40}$$

The fracture aperture and porosity, as well as cavity volume, are updated following equations (19)–(21) and (37). The matrix and fracture permeabilities are updated based on equations (11) and (22). Once the fixed-stress iteration converges, the next time step starts. The coupling convergence criterion is that the relative changes of fluid pressure and displacement at two adjacent coupling iterations are within a preset tolerance, i.e. $|\mathbf{p}^{n+1} - \mathbf{p}^{n}|/|\mathbf{p}^{n+1}| < \varepsilon$ and $|\mathbf{u}^{n+1} - \mathbf{u}^{n}|/|\mathbf{u}^{n+1}| < \varepsilon$, in which $|\ |$ denotes the norm of the vector and ε may be set as 10^{-4}. Moreover, it should be noted that the update of pore volume of matrix and fractures is achieved by fixing their grid volumes and updating the porosities, while the pore volume of cavity is updated by changing the cavity grid volume according to equation (37) with the cavity porosity

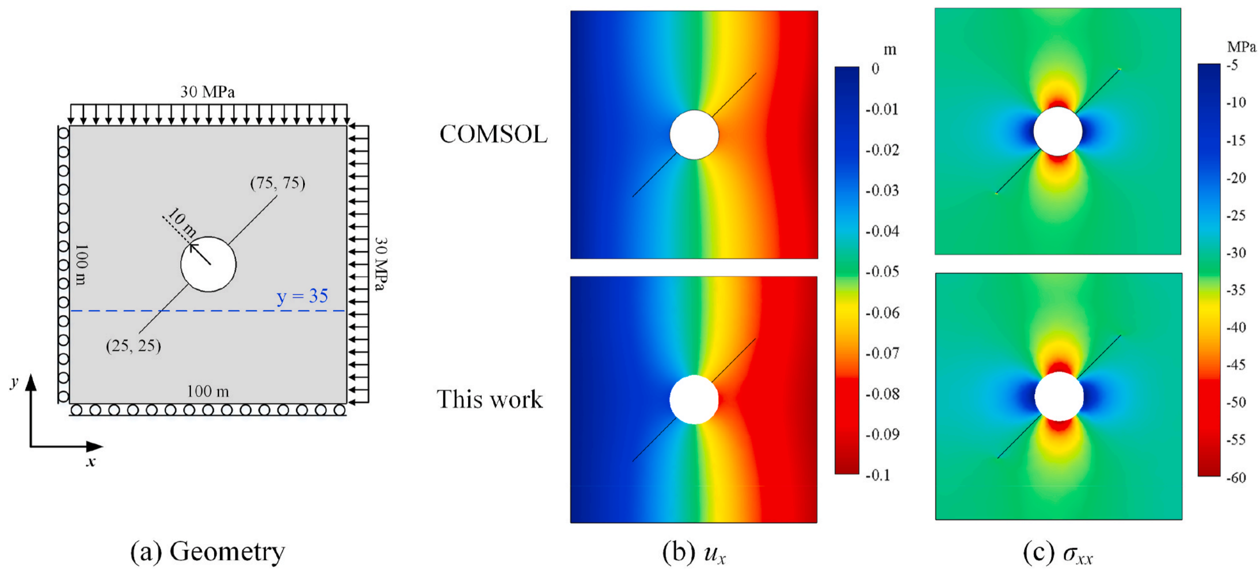

Fig. 9. (a) Geometry of the fractured karst medium, and comparison of (b) u_x and (c) σ_{xx} profiles calculated by COMSOL and this work.

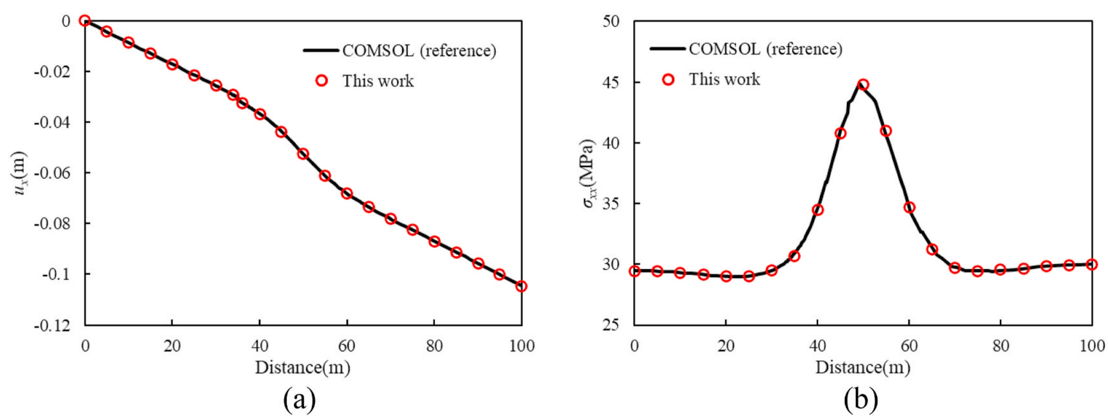

Fig. 10. Comparison of (a) u_x and (b) σ_{xx} on the line of y = 35 as shown in Fig. 9a.

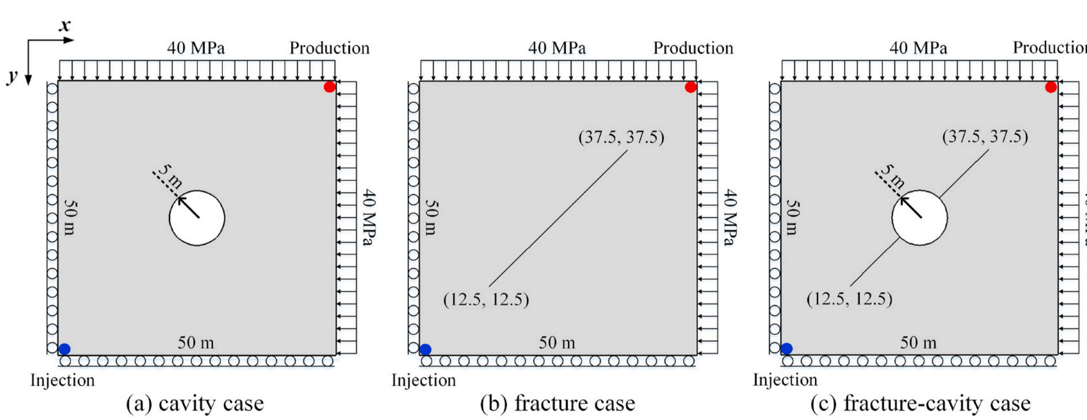

Fig. 11. Geometries for 2D (a) single-cavity, (b) single-fracture, and (c) single-fracture-cavity systems.

being 1.

The proposed model and numerical schemes provide a new modeling framework for studying the two-phase flow and geomechanical behaviors of fractured karst reservoirs. The main advantage of the methodology is to allow modeling the fully-coupled hydro-mechanical process in fractured karst reservoirs, including two-phase Darcy's flow in matrix and fractures, free flow in cavities, non-linear fracture displacement and large cavity deformation. Moreover, two-phase fluid redistribution in cavities can be efficiently solved based on the assumption of phase instantaneous gravity segregation.

Table 1
Basic parameters used in the simulation.

Matrix porosity	0.1
Matrix permeability (mD)	0.1
Matrix Young's modulus (GPa)	20
Matrix Poisson's ratio	0.27
Biot coefficients for matrix and fractures	0.3, 1
Initial fracture aperture (mm)	0.3
JRC	15
JCS (MPa)	120
Residual friction angle (°)	31
Initial pressure (MPa)	20
Initial water saturation in matrix	0.224
Pressure for production and injection (MPa)	5, 35
Water density (kg/m^3)	1000
Oil density (kg/m^3)	800
Water viscosity (mPa·s)	0.25
Oil viscosity (mPa·s)	0.4

4. Model validation and verification

In this section, three simulation cases are presented to examine the accuracy of the proposed method, regarding three different aspects. Firstly, the implementation of DFM for simulating flow in fractured porous media is verified against a widely used benchmark test obtained from Karimi-Fard et al.[70] In the second case, the proposed cavity model is validated against a physical experiment conducted by Di et al.[73] Finally, the deformation of a fractured karst medium is simulated to verify the implementation of the geomechanical model by comparing against the results of a standard finite element solver of COMSOL Multiphysics.[74] Note that the terms of "validation" and "verification" are distinguished here based on their definitions.[75]

4.1. Two-phase flow in fractured media

As shown in Fig. 7a, a model setup adapted from Karimi-Fard et al.[70] is used to verify the implementation of DFM for simulating two-phase flow in fractured porous media. Fig. 7b shows the comparison of water saturation profiles under different water injection volumes, and Fig. 7c illustrates the cumulative oil production profile. A close match is observed between our model and the one by Karimi-Fard et al.[70]

4.2. Two-phase flow in a vuggy medium

The two-phase flow experiment conducted on a closed vertical slab model with a cuboid cavity at the middle,[73] as illustrated in Fig. 8a, is used to validate the proposed cavity flow model. The porosity and absolute permeability of the porous medium are 0.53 and 8×10^{-9} m,^{2} respectively. The entire domain is initially saturated with oil. The water is injected with a constant rate of 0.45 L/min, and the production point is exposed to the atmosphere. A linear variation of relative permeability is used for the porous medium. Fig. 8b–c shows the comparison of water saturation profiles obtained from the experiment conducted by Di et al.[73] and our simulation, in which the good agreement validates our model.

4.3. Deformation of a fractured karst medium

As shown in Fig. 9a, a fractured karst medium with a fracture crossing a cavity is designed to test the geomechanical model based on the zero-thickness interface element method. The fractures are modeled by grid refinements in COMSOL and zero-thickness interface elements in our model, respectively. The Young's modulus and Poisson's ratio of the medium are 20 GPa and 0.25, respectively. The results calculated by COMSOL are used as reference. Fig. 9b–c shows the comparison of u_x and σ_{xx} profiles between the reference and our results, and the distribution of u_x and σ_{xx} on the line of y = 35 is provided in Fig. 10. The small displacement discontinuity across the fracture can be observed in Fig. 10a, and the good fits confirm the accuracy of our geomechanical model.

5. Model applications

In this section, the model developed is applied to a series of 2D and 3D problems to investigate the effect of fractures and cavities on the flow and geomechanical behaviors of fractured karst reservoirs.

5.1. 2D simple fracture-cavity systems

As shown in Fig. 11, three simple fracture-cavity systems, including single-cavity, single-fracture, and single-fracture-cavity models, are constructed to investigate the effect of an individual fracture and/or cavity on the flow and geomechanical processes in the system. The basic parameters[23,62,63] used in the simulation are summarized in Table 1. The relative permeability curves for matrix and fractures, as well as the capillary pressure curve for matrix, are shown in Fig. 12. The fracture and cavity are assumed to be initially oil-saturated due to the capillary imbibition. No-flow boundary conditions are applied on all the boundaries. Note that these parameters and characteristic curves will also be used later in sections 5.2 and 5.3. Then water-flooding simulations are conducted on the three models (as shown in Fig. 11) with the injection and production wells located at two opposite corners. A triangular gird is used to discretize the three models with the element size set as 1.5 m. The total numbers of coupling iterations are 929, 1002 and 976, and the numbers of time steps are 561, 590 and 570 for the three models, respectively, which means about two fixed-stress iterations per time step

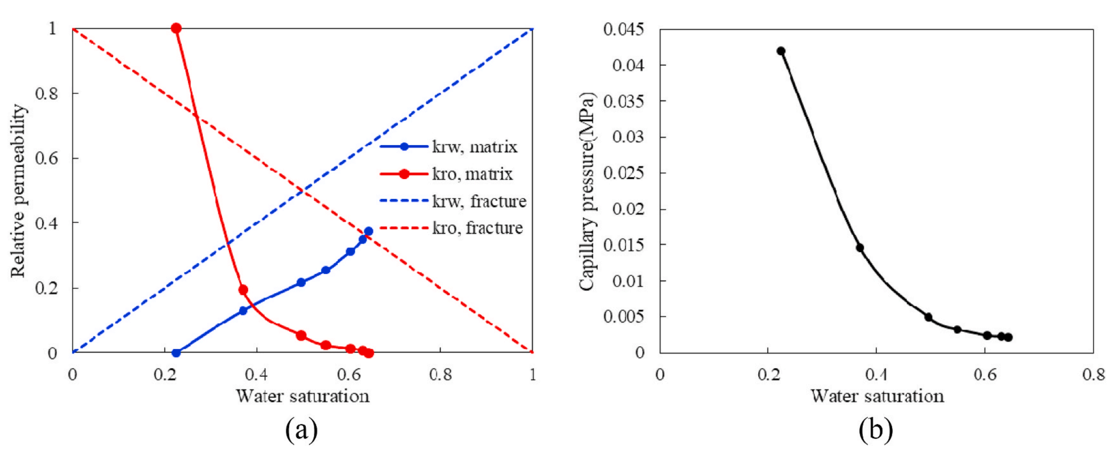

Fig. 12. (a) Relative permeability curves for matrix and fractures and (b) capillary pressure curve for matrix.

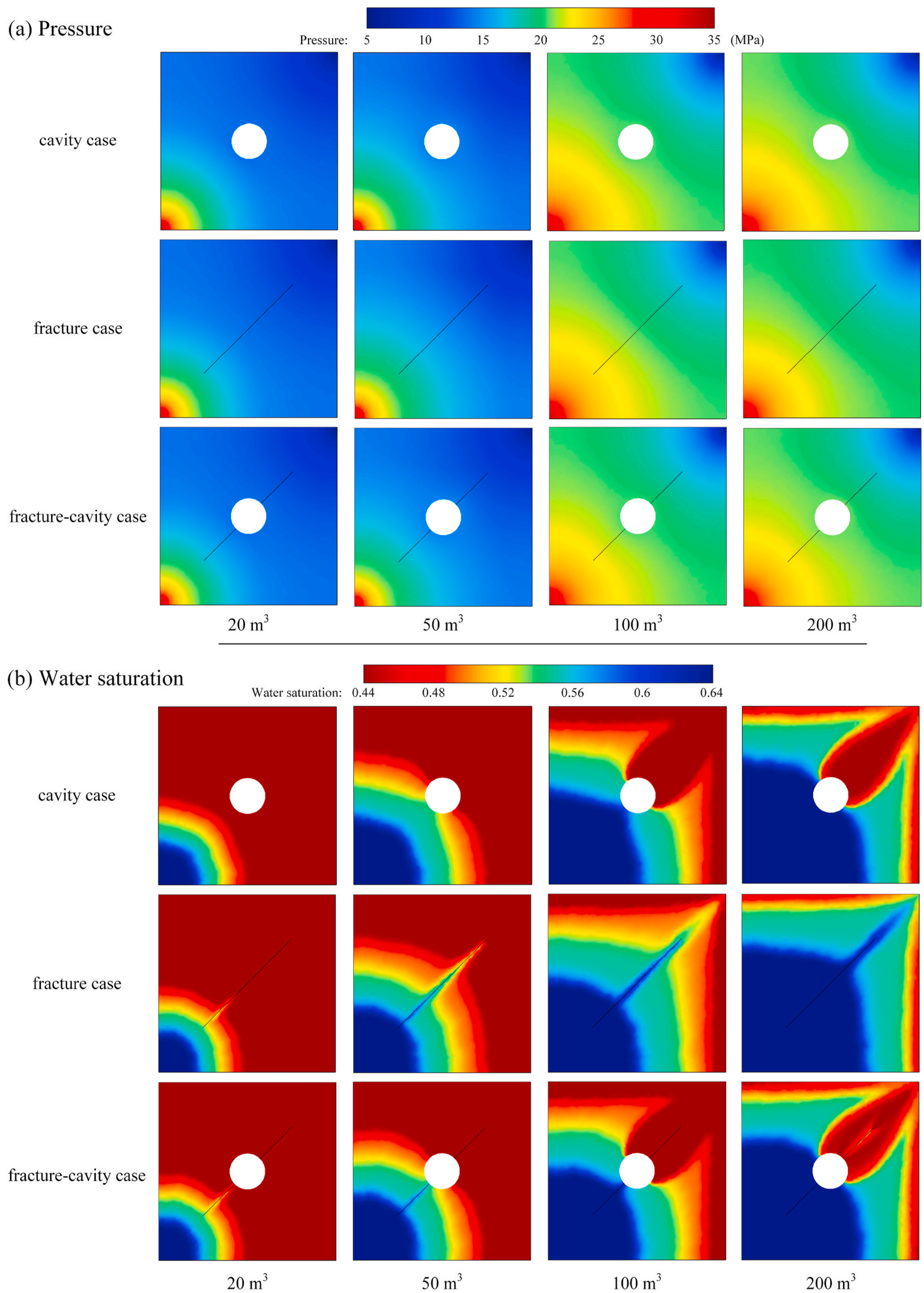

Fig. 13. Distributions of (a) pressure and (b) water saturation in matrix for 2D single-cavity, single-fracture, and single-fracture-cavity systems during the injection of 200 m^2 water.

in average. The CPU time is 515, 614 and 631 s for the three models on a PC with an Intel(R) Core(TM) i7-4790 processor.

Fig. 13 shows the distributions of pressure and water saturation in 2D simple fracture-cavity systems during the injection of 200 m^2 water. As shown in Fig. 13a, similar pressure distribution can be observed in the three cases, but pressure disperses a little slower in the single-cavity and single-fracture-cavity cases because of the stabilization of the cavity. However, significant difference can be observed when comparing the water saturation distributions in the single-cavity and single-fracture models. As shown in Fig. 13b, the cavity can hinder the water breakthrough. Water seems to flow towards the production well bypassing the cavity. This can be attributed to the storage effect of cavities. Water will

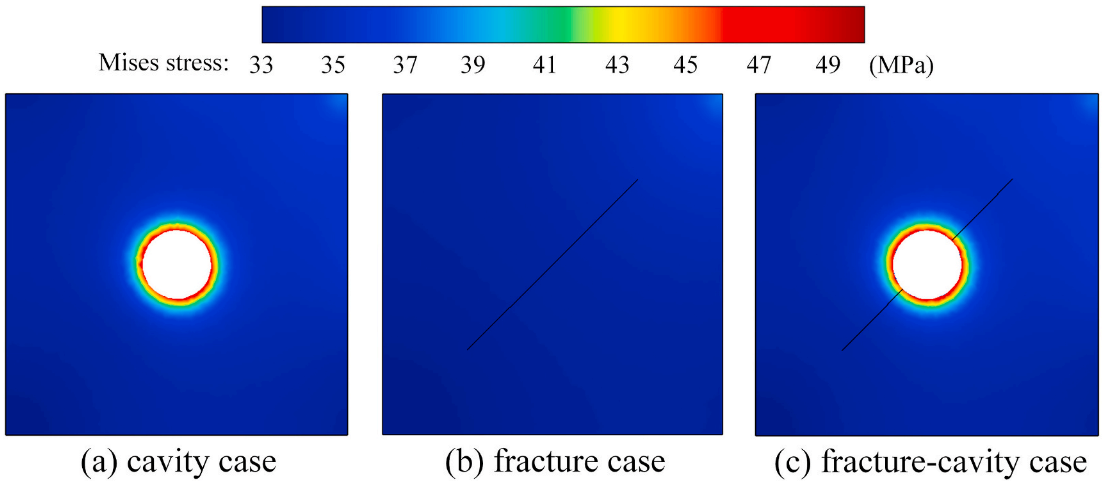

Fig. 14. Mises equivalent stress distribution for 2D (a) single-cavity, (b) single-fracture, and (c) single-fracture-cavity systems after the injection of 200 m^2 water.

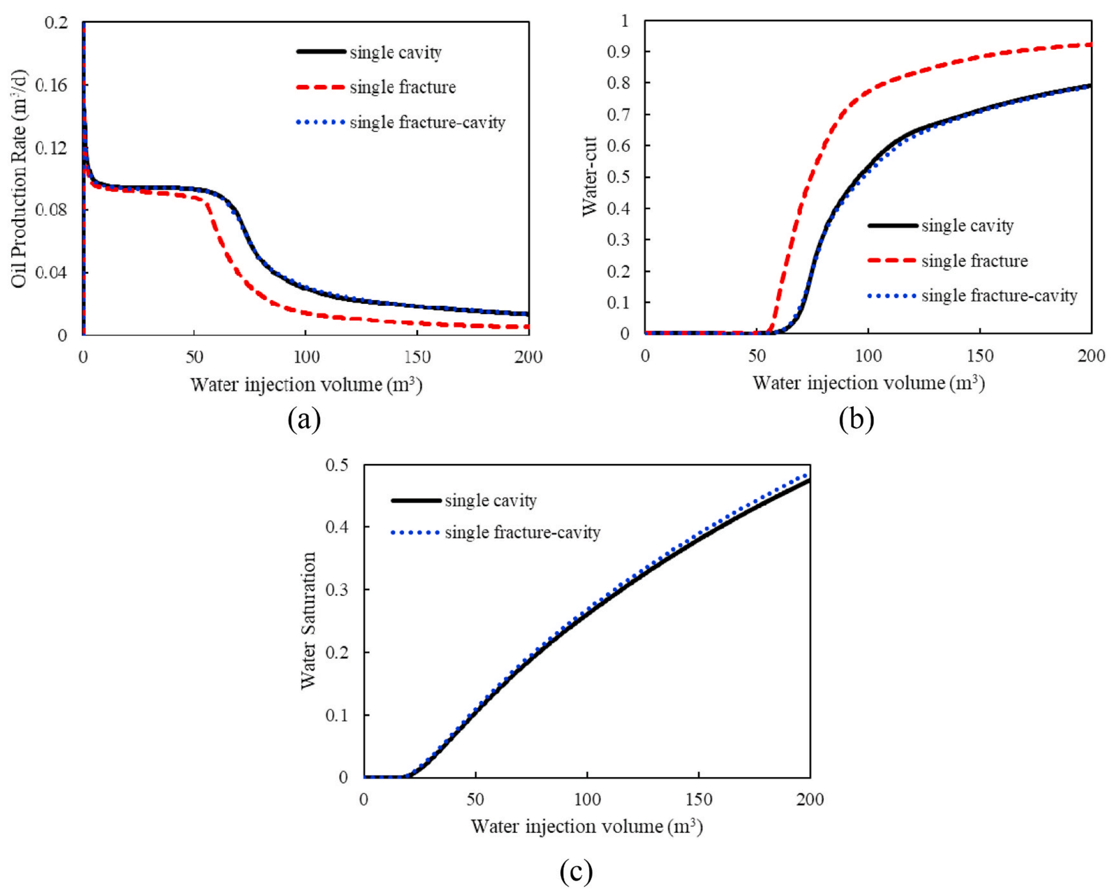

Fig. 15. Comparison of (a) oil production rate and (b) water-cut profiles among 2D single-cavity, single-fracture, and single-fracture-cavity models, and (c) water saturation evolution in the cavity of single-cavity and single-fracture-cavity models during the injection of 200 m^2 water.

be stored in the cavity when the injected water reaches to it, and water cannot completely flow through the cavity until the cavity is fully filled with water. However, this infilling processes may take a long time due to the large volume of the cavity, which can be evidenced by the slow increase of water saturation in the cavity, as illustrated in Fig. 15c. Different with the hindering effect of the cavity, the fracture promotes the water breakthrough. As shown in the middle panel of Fig. 13b, the fracture serves as a dominant flow channel, and the injected water can be efficiently transferred towards the production well through the fracture. Moreover, similar water saturation distribution can be observed in the single-fracture and single-fracture-cavity cases (middle and lower panels in Fig. 13b) before water reaches to the cavity. However, cavity gradually dominates water flow after the water reaches to the cavity, and then the water saturation distribution in the single-fracture-cavity case becomes similar to that in the single-cavity case. Fig. 14 shows the Mises equivalent stress distribution after the injection of 200 m^2 water. More obvious stress concentration is observed in the single-cavity and single-fracture-cavity models because the cavity

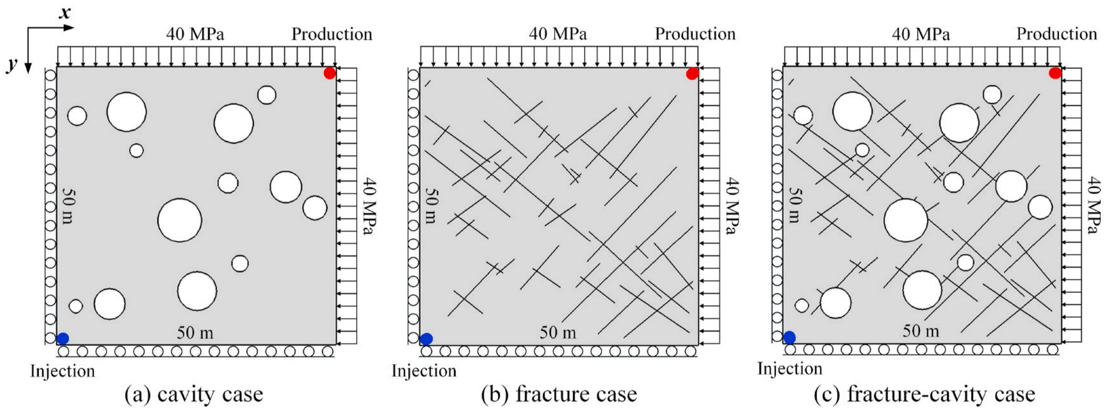

Fig. 16. Geometries for 2D (a) cavity-network, (b) fracture-network, and (c) fracture-cavity-network systems.

boundary is only supported by the fluid pressure, while the stress is more uniform in the single-fracture model because the fracture can be supported by not only the fluid pressure but its rough surfaces. The similar water saturation and stress distributions in the single-cavity and single-fracture-cavity models indicate the dominant effect of the cavity on the flow and mechanical behaviors. It should be noted that most of the above conclusions can be also drawn from a non-coupled model, but the flow and deformation details caused by the interactions between flow and geomechanics are better captured by the coupled approach.

Fig. 15a–b provides the oil production rate and water-cut profiles during the injection of 200 m^2 water. The injected water firstly reaches the production well with less water injection volume in the single-fracture model, because the fracture tends to promote the water breakthrough, while the hindering effect of the cavity delays the water breakthrough in the single-cavity and single-fracture-cavity models. Another observation from Fig. 15a and b is that the oil production rate is higher, and the water-cut is lower in the single-cavity and single-fracture-cavity models after the injected water reaches the production well. This is mainly because the cavity hinders the water breakthrough, and slows down the water production. On the other hand, the large-volume oil in cavity can be continuously supplied to the production well, which stabilizes the oil production rate. Fig. 15c shows the water saturation evolution in the cavity of the single-cavity and single-fracture-cavity models. The water saturation in the cavity is slightly higher in the single-fracture-cavity model because the injected water can flow into the cavity more efficiently through the fracture connected with the cavity.

5.2. 2D fracture-cavity network

To investigate the effect of more realistic fracture/cavity systems, three models, i.e. cavity-network, fracture-network, and fracture-cavity-network models, are established, as illustrated in Fig. 16. In the cavity-network model, the cavities are randomly generated with the cavity radius following an exponential distribution with the mean radius being 5 m. The volumetric fraction of cavities is 0.1. In the fracture-network model, two sets of fractures oriented approximately 45° and 140° are generated. The fracture length follows an exponential distribution, while the mean fracture length is set to be 8 m. The fracture-cavity-network model is generated by combining the cavity-network and fracture-network models. A triangular grid is used to discretize the three models with the element size set as 1.5 m. The total numbers of coupling iterations are 1156, 1015 and 1118, and the numbers of time steps are 510, 575 and 497 for the cavity-network, fracture-network, and fracture-cavity-network models, respectively. The CPU time is 1963, 1722 and 3437 s for the three models on the same PC as used in subsection 5.1.

Fig. 17 presents the distributions of pressure and water saturation in 2D fracture-cavity network systems during the injection of 200 m^2 water. As shown in Fig. 17a and compared with the cases of simple fracture-cavity structures (i.e. Fig. 13b), much slower pressure dispersion can be observed in the cavity-network and fracture-cavity-network cases due to the enlarged cavity volumes. Moreover, more complex water saturation distribution patterns can be observed in Fig. 17b. Because of the hindering effect of the randomly distributed cavities, the water-flow paths become tortuous in the cavity-network model, as illustrated in upper panel of Fig. 17b. Large amount of oil still remains behind the cavities, because the injected water cannot completely flow through the cavities. Similar water saturation profile is also observed in the fracture-cavity-network model, i.e. lower panel of Fig. 17b. However, water distribution is more non-uniform in the fracture-cavity-network model since the fractures act as high-conductivity water-flow channels, which accordingly lead to higher water saturation in the vicinity of fractures. Differently, as shown in middle panel of Fig. 17b, water quickly breaks through in the fracture-network system. Almost the entire domain can be swept by the injected water due to the spatially distributed fractures. In addition, significant stress concentration can be observed when cavities are present, and the interaction between fractures and cavities can further intensify the non-uniformity of stress, as evidenced by Fig. 18.

Fig. 19 shows the oil production rate and water-cut profiles during the water injection. The overall production patterns are similar with those of simple fracture-cavity structures (i.e. Fig. 15). However, two differences can be observed. Firstly, the injected water reaches the production well much earlier in the fracture-network model. This can be attributed to the higher conductivity of the fracture network, and the enhanced hindering effect of the cavity network. The other difference is that the water-cut is much lower in the cavity-network and fracture-cavity-network models than that in fracture-network model, which can be also attributed to the enhanced hindering effect of the enlarged cavity volume.

Moreover, various-sized cavities may be distributed in fractured karst reservoirs even with the same total cavity volumes.[7] To investigate the effect of cavity size distribution on the flow and geomechanical behaviors, two models dominated by large-sized cavities and small-sized cavities are constructed as shown in Fig. 20, and the model (c) in Fig. 16 dominated by medium-sized cavities is used for comparison. The total cavity volumes are same in the three models.

Fig. 21 illustrates the distributions of pressure and water saturation in fractured karst models dominated by different-sized cavities during water injection. As shown in Fig. 21 and compared with the medium-sized cavity case (i.e. lower panels of Fig. 17a and b), pressure disperses faster and water breaks through more quickly in the large-sized cavity dominated model. This is because that with the same total cavity volumes, cavities become more localized when the cavity size becomes large. In that case, preferential flow paths for injected water are

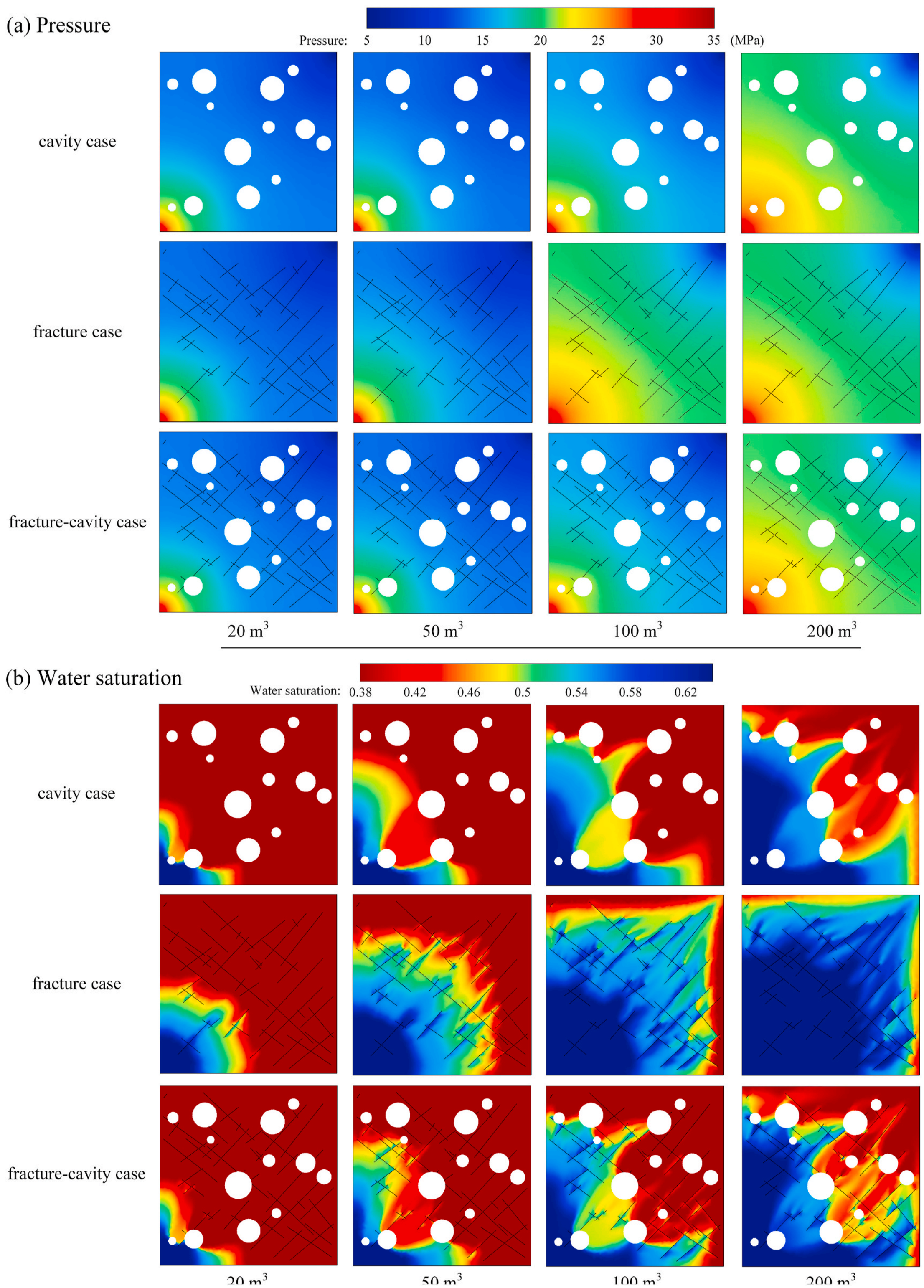

Fig. 17. Distributions of (a) pressure and (b) water saturation in matrix for 2D cavity-network, fracture-network, and fracture-cavity-network systems during the injection of 200 m^2 water.

more likely to be formed. However, the injected water can be hindered by the well distributed cavities in the small-sized cavity dominated model, as illustrated in Fig. 21b. Furthermore, it can be found in Fig. 22 that stress concentration is more obvious around the large-sized cavities. Fig. 23 presents the oil production rate and water-cut profiles of models dominated by different-sized cavities. Lower oil production rate and higher water cut are observed when the model is dominated by larger-sized cavities.

5.3. 3D fracture-cavity network

To show the applicability of our proposed model for 3D complex fractured karst porous media, two 3D models, i.e. fracture-network and fracture-cavity-network models, are constructed, as shown in Fig. 24. In

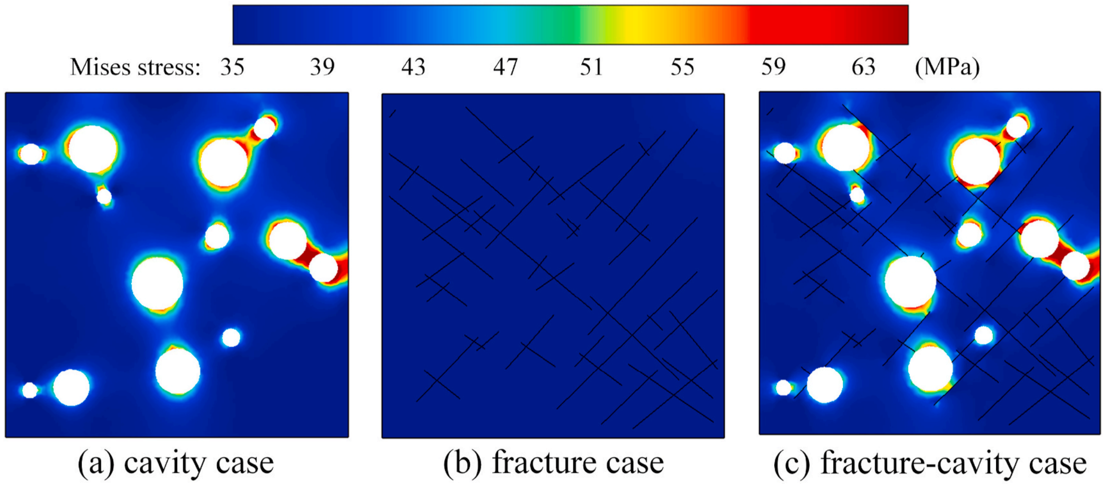

Fig. 18. Mises equivalent stress distribution for 2D (a) cavity-network, (b) fracture-network, and (c) fracture-cavity-network systems after the injection of 200 m^2 water.

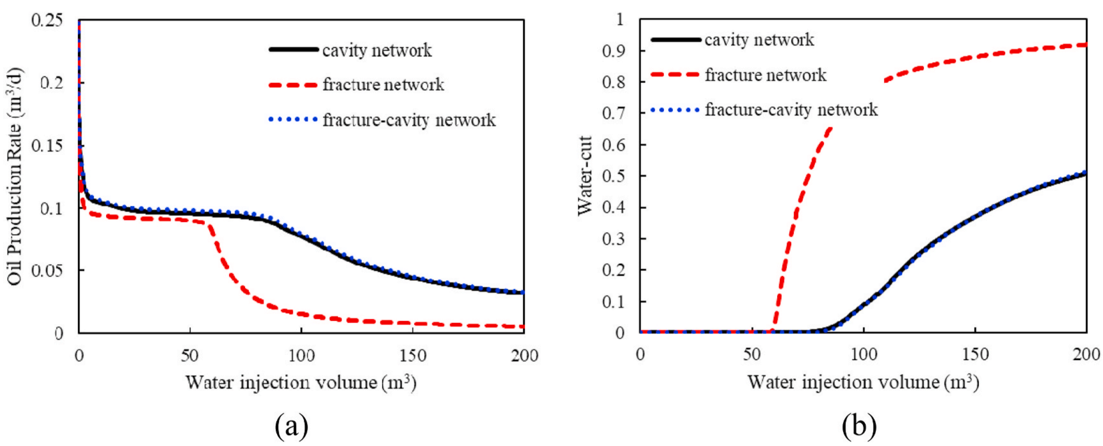

Fig. 19. Comparison of (a) oil production rate and (b) water-cut profiles among 2D cavity-network, fracture-network, and fracture-cavity-network models during the injection of 200 m^2 water.

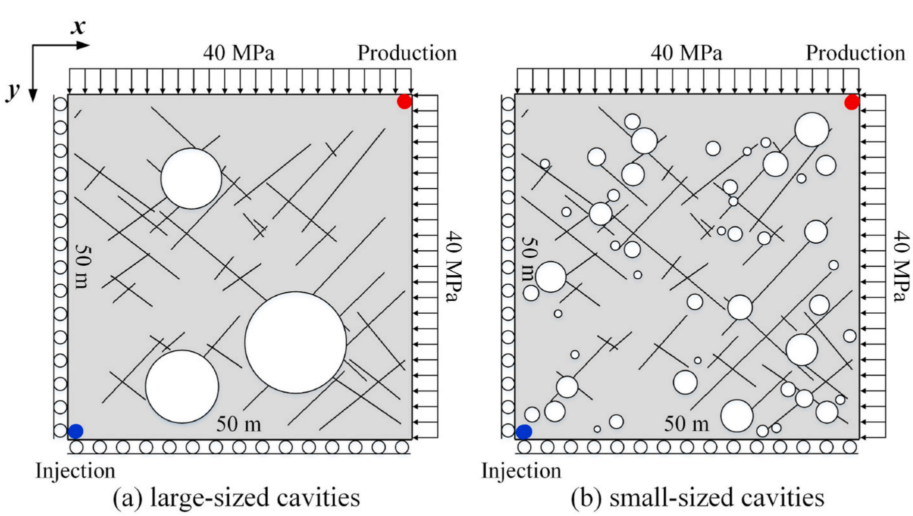

Fig. 20. Geometries for fracture-cavity-network systems dominated by (a) large-sized cavities and (b) small-sized cavities.

these two models, the five orthogonal fractures are manually generated, and the two cavities have the same volume of 1200 m^3. The stress boundary condition is applied to the right, back, and bottom boundaries with the vertical stress $S_z = 60$ MPa, and the horizontal stress $S_{x(y)} = 40$ MPa. The roller constraint boundary condition is adopted to the opposing three boundaries. A structured grid is used for the spatial

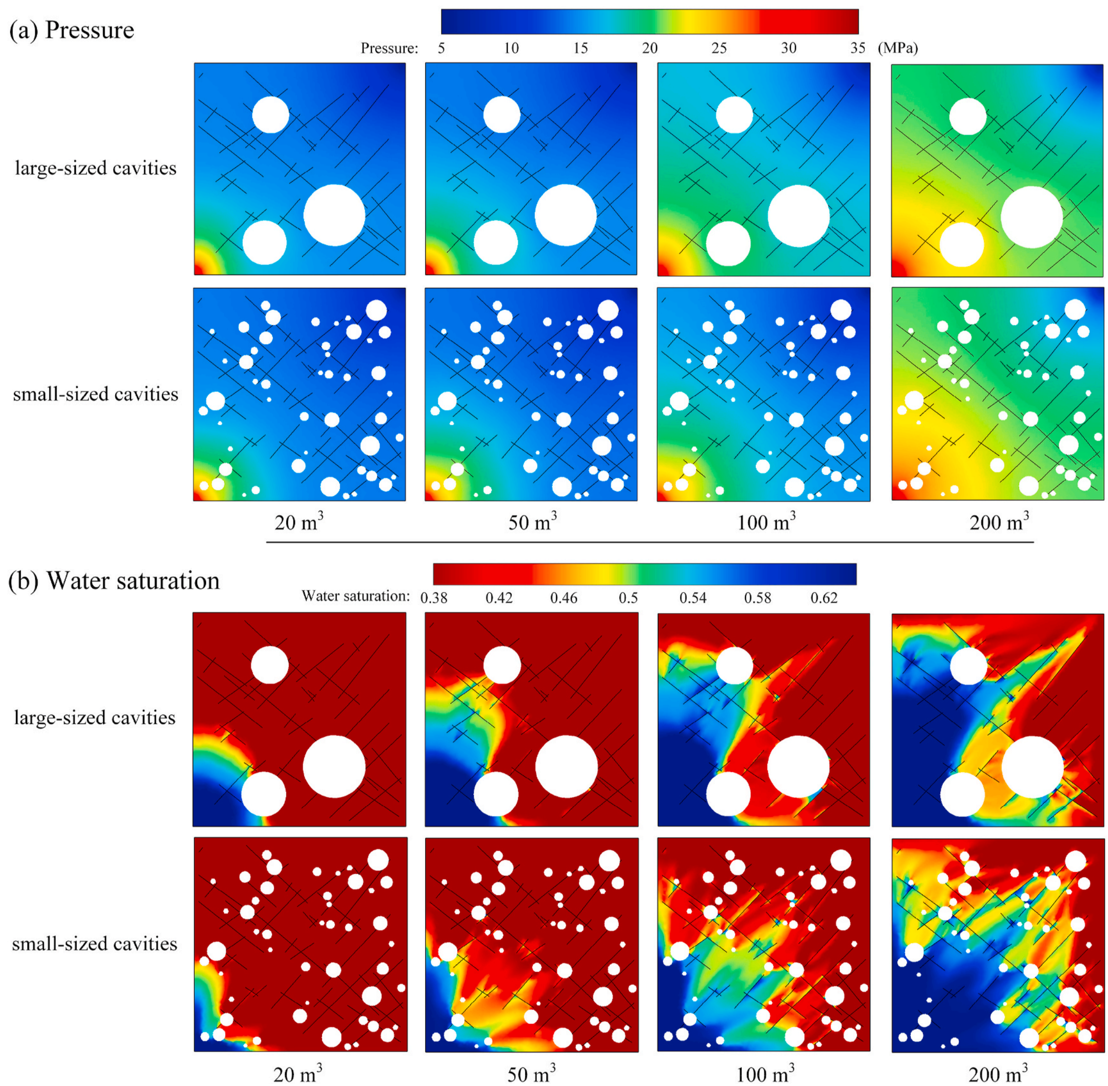

Fig. 21. Distributions of (a) pressure and (b) water saturation in matrix for 2D fracture-cavity-network systems dominated by different-sized cavities during the injection of 200 m^2 water.

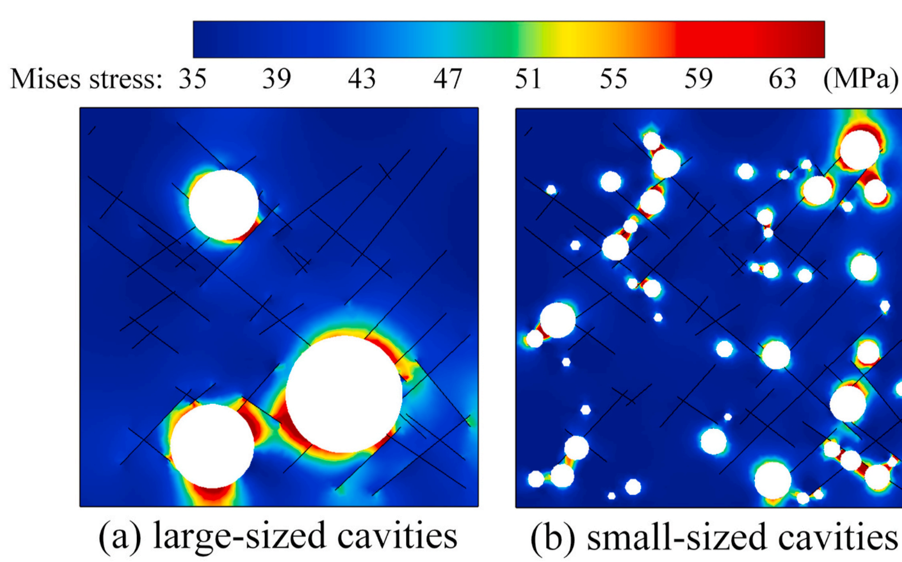

Fig. 22. Mises equivalent stress distribution for 2D fracture-cavity-network systems dominated by (a) large-sized cavities and (b) small-sized cavities after the injection of 200 m^2 water.

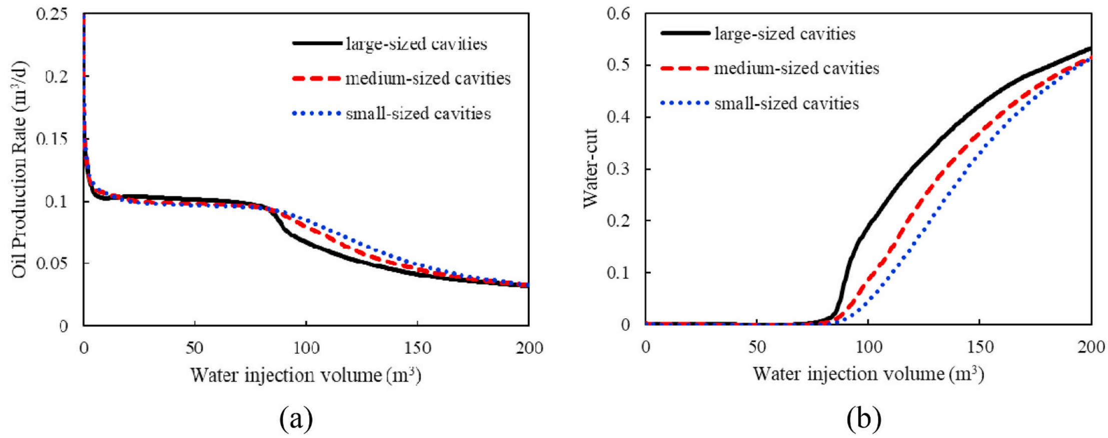

Fig. 23. Comparison of (a) oil production rate and (b) water-cut profiles among fracture-cavity models dominated by different-sized cavities during the injection of 200 m^2 water.

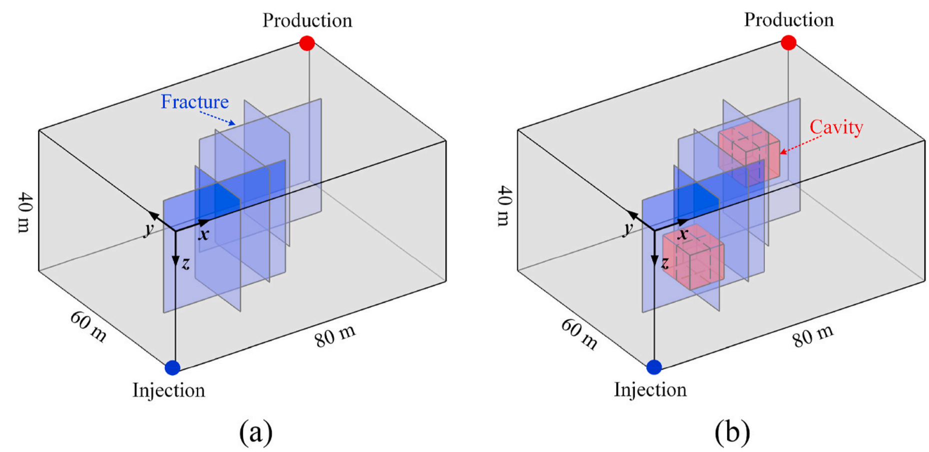

Fig. 24. Geometries of 3D (a) fracture-network, and (b) fracture-cavity-network models.

discretization, and the grid size is set as 2 m. The total numbers of coupling iterations are 368 and 513, and the numbers of time steps are both 279 for the fracture-network and fracture-cavity-network models, respectively. The CPU time is 15,871 and 21,678 s for the two models on the same PC as used in subsection 5.1.

Fig. 25a–b compares the distributions of pressure and water saturation in matrix during the injection of 10,000 m^3 water, and the corresponding water saturation distribution in fractures is shown in Fig. 25c. Obviously, the hindering effect of the cavities can be still observed, which is evidenced by the higher oil saturation surrounding the production well in the fracture-cavity-network model. Furthermore, gravity has a significant impact on the water saturation distribution. As shown in the lower panel of Fig. 25b, the water saturation is lower in the area above the two cavities because under the effect of gravity, water cannot flow out from the top of the cavities until the cavities are fully saturated by water. Similar to the 2D models, there is a strong stress concentration when cavities are present, while the stress is more uniform in the fracture-network model (see Fig. 26).

Fig. 27a–b shows the oil production rate and water-cut profiles during the injection of 10,000 m^3 water. It is obvious that, compared to the fracture-network model, the oil production rate is higher and the water-cut is lower in the fracture-cavity-network model after water breakthrough, and the explanation is similar with that in section 5.2. Moreover, Fig. 27c provides the water saturation evolution in the two cavities of the fracture-cavity-network model. Apparently, the injected water firstly flows into the lower cavity, and the water saturation in the lower cavity starts to increase almost at the beginning. Then, the water saturation in the upper cavity begins to increase when water reaches after a large amount of water injection.

6. Conclusions

In this study, a novel and efficient coupled hydro-mechanical model is developed to simulate two-phase flow and geomechanics in fractured karst porous media. The proposed model takes into account two-phase Darcy flow in porous matrix and fractures, free flow in cavities, nonlinear fracture deformation and cavity deformation as well as the coupling between flow and geomechanics. The model has been validated against some existing numerical and experimental results, and its capability of simulating coupled two-phase flow and geomechanics in complex fractured karst porous media has been further demonstrated based on a series of 2D and 3D case studies. The following conclusions can be drawn from our simulation results: (1) cavities hinder water breakthrough due to the storage effect, while water can break through quickly via high-conductivity fractures; (2) strong stress concentrations can be observed when cavities are present; (3) cavities dominate the flow and geomechanical behaviors when fractures and cavities coexist; (4) with the same total cavity volumes, water tends to break through more quickly in the model dominated by large-sized cavities due to more localized cavity configuration; (5) gravity tends to have an important impact on the water saturation distribution in 3D systems: water saturation is often low in the area above cavities during water flooding. Future work will focus on further considering the cavity shape change due to the large stress acting on the cavity boundaries by using the finite

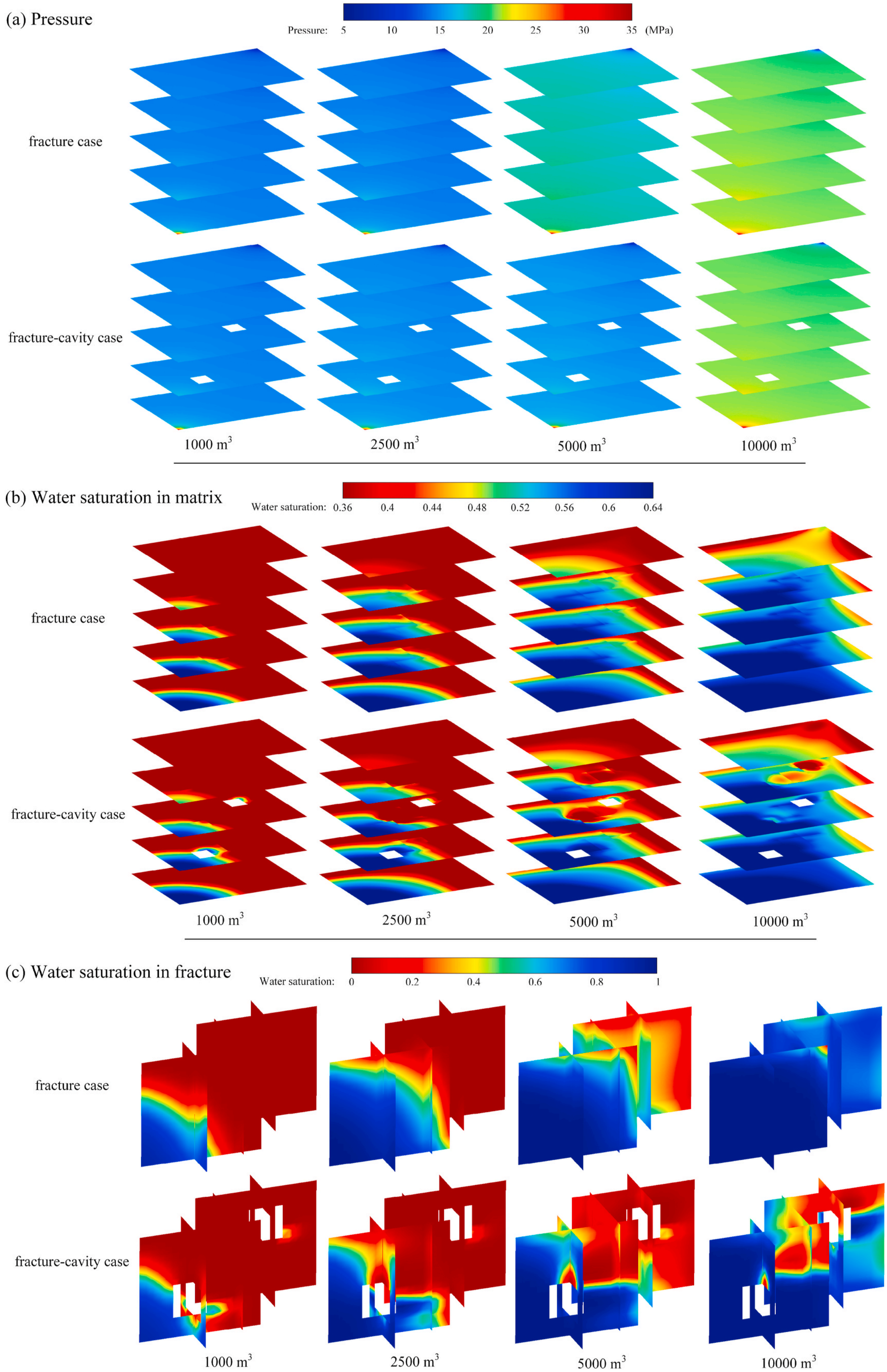

Fig. 25. Distributions of (a) pressure, (b) water saturation in matrix, and (c) water saturation in fractures for 3D fracture-network and fracture-cavity-network models during the injection of 10,000 m^3 water. The profiles for matrix are shown in five layers with a spacing of 10 m. The length in the z-direction is shown twice the real size.

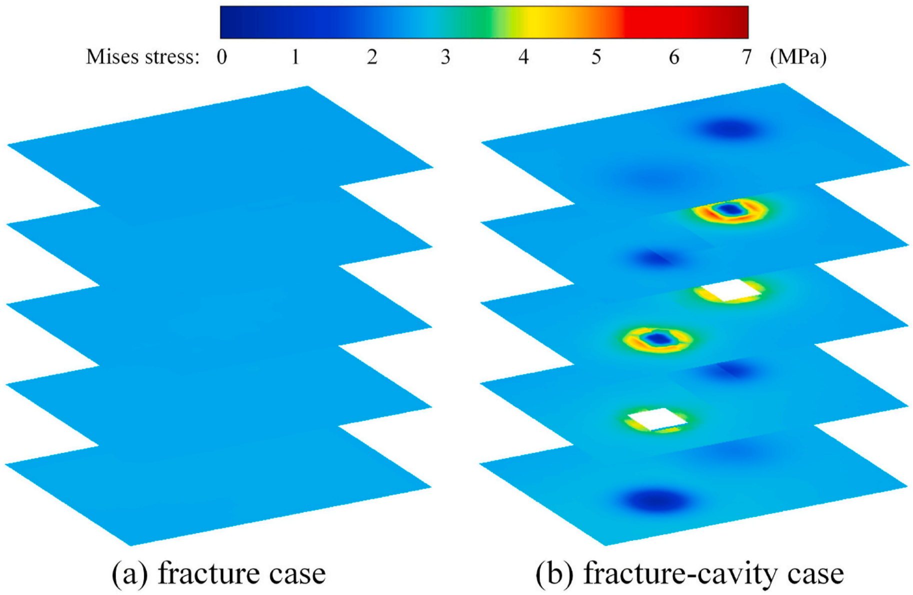

Fig. 26. Mises equivalent stress distribution for 3D (a) fracture-network, and (b) fracture-cavity-network models after the injection of 10,000 m^3 water.

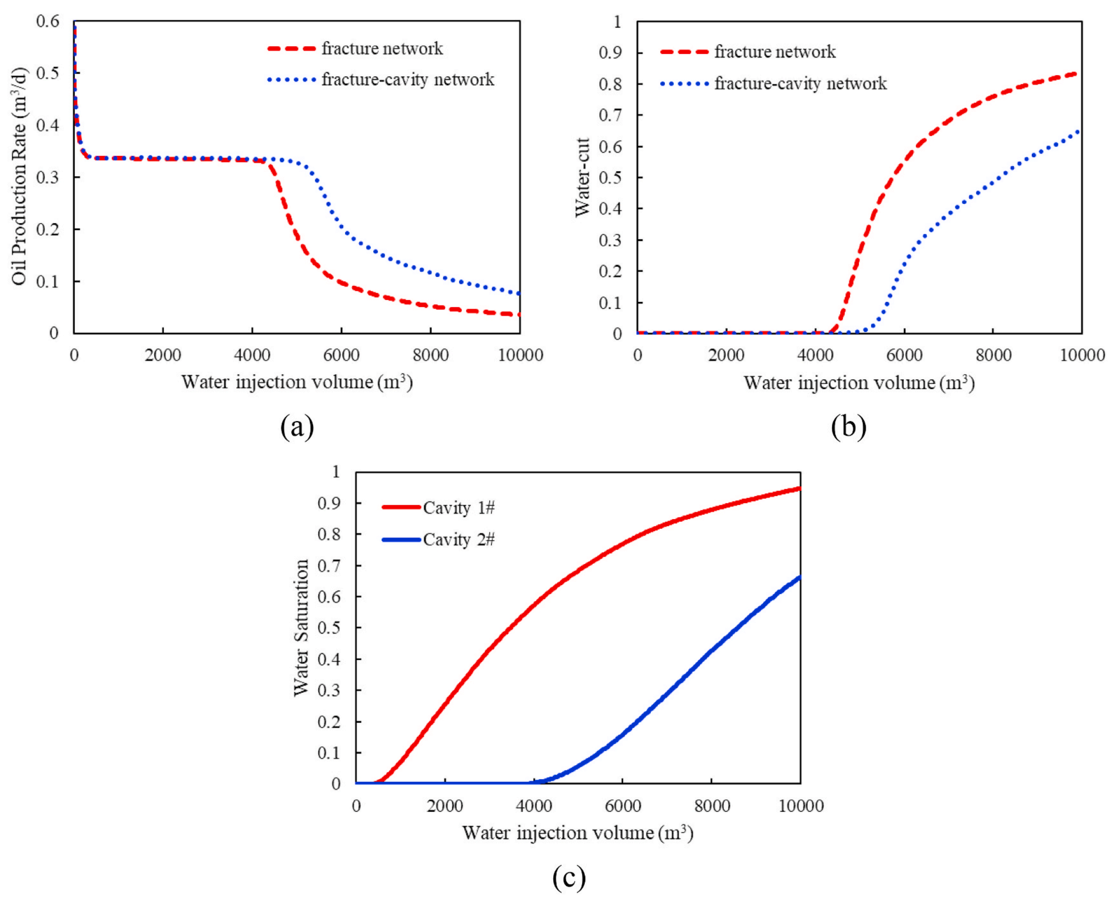

Fig. 27. Comparison of (a) oil production rate and (b) water-cut profiles between 3D fracture-network and fracture-cavity-network models during the injection of 10,000 m^3 water, and (c) water saturation evolution in the two cavities of the fracture-cavity-network model. Cavity 1# is the lower cavity, and cavity 2# is the upper one.

deformation theory. Moreover, the Navier-Stokes equations may be required for more accurately modeling the free flow in cavities, since the assumption of phase instantaneous gravity segregation is not valid under turbulent flow.

Declaration of competing interest

The authors declare that they have no known competing financial interests or personal relationships that could have appeared to influence the work reported in this paper.

Acknowledgments, Samples, and Data

The authors would like to thank the support of the National Science and Technology Major Project (2017ZX05009-001), Major science and technology projects of China National Petroleum Corporation (ZD2019-183-008), National Nature Science Foundation of China (52074336, 52004321, 51722406, 51804325), Shandong Provincial Natural Science Foundation (JQ201808), China Postdoctoral Science Foundation (2020M682265, 2019M652508), Qingdao Postdoctoral Applied Research Project (qdyy20190025), and Fundamental Research Funds for the Central Universities (20CX06025A, 18CX05029A).

References

1 Okabe H, Blunt MJ. Pore space reconstruction of vuggy carbonates using microtomography and multiple-point statistics. *Water Resour Res*. 2007;43(12): W12S02.
2 Yong L, Baozhu L, Hui P, Fangfang C. An integrated dynamic characterization and performance prediction method for fractured-vuggy carbonate reservoirs. In: *International Petroleum Technology Conference*. 2016. https://doi.org/10.2523/IPTC-18609-MS. International Petroleum Technology Conference.
3 Popov P, Efendiev Y, Qin G. Multiscale modeling and simulations of flows in naturally fractured karst reservoirs. *Commun Comput Phys*. 2009;6(1):162–184.
4 Huang Z, Yao J, Li Y, Wang C, Lv X. Numerical calculation of equivalent permeability tensor for fractured vuggy porous media based on homogenization theory. *Commun Comput Phys*. 2011;9(1):180–204.
5 Golfier F, Lasseux D, Quintard M. Investigation of the effective permeability of vuggy or fractured porous media from a Darcy-Brinkman approach. *Comput Geosci*. 2015;19 (1):63–78.
6 Camacho-Velazquez R, Vasquez-Cruz M, Castrejon-Aivar R, Arana-Ortiz V. Pressure transient and decline curve behaviors in naturally fractured vuggy carbonate reservoirs. In: *SPE Annual Technical Conference and Exhibition*. Society of Petroleum Engineers; 2002. https://doi.org/10.2118/77689-MS.
7 Wu Y-S, Di Y, Kang Z, Fakcharoenphol P. A multiple-continuum model for simulating single-phase and multiphase flow in naturally fractured vuggy reservoirs. *J Petrol Sci Eng*. 2011;78(1):13–22.
8 Girault V, Rivière B. DG approximation of coupled Navier–Stokes and Darcy equations by Beaver–Joseph–Saffman interface condition. *SIAM J Numer Anal*. 2009; 47(3):2052–2089.
9 Yao J, Huang Z, Li Y, Wang C, Lv X. Discrete fracture-vug network model for modeling fluid flow in fractured vuggy porous media. In: *International Oil and Gas Conference and Exhibition in China*. Society of Petroleum Engineers; 2010. https://doi.org/10.2118/130287-MS.
10 Liu L, Huang Z, Yao J, Di Y, Wu Y-S. An efficient hybrid model for 3D complex fractured vuggy reservoir simulation. *SPE J*. 2020;25(2):907–924.
11 Zhang Q, Huang Z, Yao J, Wang Y, Li Y. A multiscale mixed finite element method with oversampling for modeling flow in fractured reservoirs using discrete fracture model. *J Comput Appl Math*. 2017;323:95–110.
12 Zhang N, Yao J, Xue S, Huang Z. Multiscale mixed finite element, discrete fracture–vug model for fluid flow in fractured vuggy porous media. *Int J Heat Mass Tran*. 2016;96:396–405.
13 Saffman PG. On the boundary condition at the surface of a porous medium. *Stud Appl Math*. 1971;50(2):93–101.
14 Beavers GS, Joseph DD. Boundary conditions at a naturally permeable wall. *J Fluid Mech*. 1967;30(1):197–207.
15 Chen J, Sun S, Chen Z. Coupling two-phase fluid flow with two-phase Darcy flow in anisotropic porous media. *Adv Mech Eng*. 2014;6:871021.
16 Huang ZQ, Gao B, Zhang XY, Yao J. On the coupling of two-phase free flow and porous flow. In: *ECMOR XV-15th European Conference on the Mathematics of Oil Recovery*. European Association of Geoscientists & Engineers; 2016. cp-494.
17 Xie H, Li A, Huang Z, Gao B, Peng R. Coupling of two-phase flow in fractured-vuggy reservoir with filling medium. *Open Phys*. 2017;15(1):12–17.
18 Zhu G, Kou J, Yao B, Wu YS, Yao J, Sun S. Thermodynamically consistent modelling of two-phase flows with moving contact line and soluble surfactants. *J Fluid Mech*. 2019;879:327–359.
19 Chen W, Han D, Wang X. Uniquely solvable and energy stable decoupled numerical schemes for the Cahn–Hilliard–Stokes–Darcy system for two-phase flows in karstic geometry. *Numer Math*. 2017;137(1):229–255.
20 Song W, Liu L, Wang D, Li Y, Prodanović M, Yao J. Nanoscale confined multicomponent hydrocarbon thermodynamic phase behavior and multiphase transport ability in nanoporous material. *Chem Eng J*. 2020;382:122974.
21 Gao Y, He X, Mei L, Yang X. Decoupled, linear, and energy stable finite element method for the Cahn-Hilliard-Navier-Stokes-Darcy phase field model. *SIAM J Sci Comput*. 2018;40(1):B110–B137.
22 Goodman RE. *Methods of Geological Engineering in Discontinuous Rocks*. San Francisco, CA: West Publishing Company; 1976.
23 Bandis SC, Lumsden AC, Barton NR. Fundamentals of rock joint deformation. *Int J Rock Mech Min Sci Geomech Abstr*. 1983;20:249–268. Pergamon.
24 Barton N, Bandis S, Bakhtar K. Strength, deformation and conductivity coupling of rock joints. *Int J Rock Mech Min Sci Geomech Abstr*. 1985;22:121–140. Elsevier.
25 Barton N, Bandis SC. Rock joint model for analyses of geologic discontinua. In: *Proc. 2 rid Int. Conf. On Constitutive Laws for Engng Materials*. Tucson, AZ: Elsvier; 1987.
26 Amadei B, Saeb S. Constitutive models of rock joints. In: *International Symposium on Rock Joints. Loen, Norway: A.A. Balkema*. 1990:581–594.
27 Jing L, Nordlund E, Stephansson O. A 3-D constitutive model for rock joints with anisotropic friction and stress dependency in shear stiffness. *Int J Rock Mech Min Sci Geomech Abstr*. 1994;31:173–178. Elsevier.
28 Asadollahi P, Invernizzi MCA, Addotto S, Tonon F. Experimental validation of modified Barton's model for rock fractures. *Rock Mech Rock Eng*. 2010;43(5): 597–613.
29 Asadollahi P, Tonon F. Constitutive model for rock fractures: revisiting Barton's empirical model. *Eng Geol*. 2010;113(1-4):11–32.
30 Min K-B, Jing L. Numerical determination of the equivalent elastic compliance tensor for fractured rock masses using the distinct element method. *Int J Rock Mech Min Sci*. 2003;40(6):795–816.
31 Min K-B, Rutqvist J, Tsang C-F, Jing L. Stress-dependent permeability of fractured rock masses: a numerical study. *Int J Rock Mech Min Sci*. 2004;41(7):1191–1210.
32 Garipov TT, Karimi-Fard M, Tchelepi HA. Discrete fracture model for coupled flow and geomechanics. *Comput Geosci*. 2016;20(1):149–160.
33 Jiang J, Yang J. Coupled fluid flow and geomechanics modeling of stress-sensitive production behavior in fractured shale gas reservoirs. *Int J Rock Mech Min Sci*. 2018; 101:1–12.
34 Liu Y, Liu L, Leung J-Y, Moridis G-J. Sequentially coupled flow and geomechanical simulation with a discrete fracture model for analyzing fracturing fluid recovery and distribution in fractured ultra-low permeability gas reservoirs. *J Petrol Sci Eng*. 2020; 189:107042.
35 Liu Y, Liu L, Leung J-Y, Wu K, Moridis G-J. Coupled flow/geomechanics modeling of interfracture water injection to enhance oil recovery in tight reservoirs. *SPE J*. 2020. https://doi.org/10.2118/199983-PA. preprint.
36 Liu L, Liu Y, Yao J, Huang Z. Efficient coupled multiphase-flow and geomechanics modeling of well performance and stress evolution in shale-gas reservoirs considering dynamic fracture properties. *SPE J*. 2020;25(3):1523–1542.
37 Lei Q, Latham J-P, Xiang J, Tsang C-F. Role of natural fractures in damage evolution around tunnel excavation in fractured rocks. *Eng Geol*. 2017;231:100–113.
38 Lei Q, Latham J-P, Tsang C-F. The use of discrete fracture networks for modelling coupled geomechanical and hydrological behaviour of fractured rocks. *Comput Geotech*. 2017;85:151–176.
39 Yan X, Huang Z, Yao J, et al. An efficient numerical hybrid model for multiphase flow in deformable fractured-shale reservoirs. *SPE J*. 2018;23:1–412, 04.
40 Zeng Q-D, Yao J, Shao J. Study of hydraulic fracturing in an anisotropic poroelastic medium via a hybrid EDFM-XFEM approach. *Comput Geotech*. 2019;105:51–68.
41 Zeng Q, Yao J, Shao J. An extended finite element solution for hydraulic fracturing with thermo-hydro-elastic–plastic coupling. *Comput Methods Appl Mech Eng*. 2020; 364:112967. https://doi.org/10.1016/j.cma.2020.112967.
42 Segura JM, Carol I. Coupled HM analysis using zero-thickness interface elements with double nodes. Part I: theoretical model. *Int J Numer Anal Methods GeoMech*. 2008;32(18):2083–2101.
43 Lewandowska J, Auriault J. Extension of Biot theory to the problem of saturated microporous elastic media with isolated cracks or/and vugs. *Int J Numer Anal Methods GeoMech*. 2013;37(16):2611–2628.
44 Yan X, Huang Z, Yao J, et al. Numerical simulation of hydro-mechanical coupling in fractured vuggy porous media using the equivalent continuum model and embedded discrete fracture model. *Adv Water Resour*. 2019;126:137–154.
45 Zhang F, An M, Yan B, Wang Y, Han Y. A novel hydro-mechanical coupled analysis for the fractured vuggy carbonate reservoirs. *Comput Geotech*. 2019;106:68–82.
46 Kim J, Tchelepi H-A, Juanes R. Stability and convergence of sequential methods for coupled flow and geomechanics: fixed-stress and fixed-strain splits. *Comput Methods Appl Mech Eng*. 2011;200(13-16):1591–1606.
47 Kim J, Moridis G, Yang D, Rutqvist J. Numerical studies on two-way coupled fluid flow and geomechanics in hydrate deposits. *SPE J*. 2012;17(2):485–501.
48 Blanco-Martín L, Rutqvist J, Birkholzer J-T. Extension of TOUGH-FLAC to the finite strain framework. *Comput Geosci*. 2017;108:64–71.
49 Both J-W, Borregales M, Nordbotten J-M, Kumar K, Radu F-A. Robust fixed stress splitting for Biot's equations in heterogeneous media. *Appl Math Lett*. 2017;68: 101–108.
50 Both J-W, Kumar K, Nordbotten J-M, Radu F-A. Anderson accelerated fixed-stress splitting schemes for consolidation of unsaturated porous media. *Comput Math Appl*. 2019;77(6):1479–1502.
51 Borregales M, Kumar K, Radu F-A, Rodrigo C, Gaspar F-J. A partially parallel-in-time fixed-stress splitting method for biot's consolidation model. *Comput Math Appl*. 2019; 77(6):1466–1478.
52 Dana S, Ganis B, Wheeler MF. A multiscale fixed stress split iterative scheme for coupled flow and poromechanics in deep subsurface reservoirs. *J Comput Phys*. 2018; 352:1–22.
53 Rutqvist J, Wu Y-S, Tsang C-F, Bodvarsson G. A modeling approach for analysis of coupled multiphase fluid flow, heat transfer, and deformation in fractured porous rock. *Int J Rock Mech Min Sci*. 2002;39(4):429–442.
54 Obeysekara A, Lei Q, Salinas P, et al. Modelling stress-dependent single and multi-phase flows in fractured porous media based on an immersed-body method with mesh adaptivity. *Comput Geotech*. 2018;103:229–241.
55 Leverett M. Capillary behavior in porous solids. *Trans AIME*. 1941;142(1):152–169.
56 Cheng AH-D. *Poroelasticity*. Berlin: Springer; 2016.
57 Salimzadeh S, Khalili N. A three-phase XFEM model for hydraulic fracturing with cohesive crack propagation. *Comput Geotech*. 2015;69:82–92.

58 Geertsma J. The effect of fluid pressure decline on volumetric changes of porous rocks. *SPE J*. 1957;210:331–340.
59 Carman P-C. Determination of the specific surface of powders I. Transactions. *J Soc Chem Ind*. 1938;57:225–234.
60 Petunin V-V, Yin X, Tutuncu A-N. Porosity and permeability changes in sandstones and carbonates under stress and their correlation to rock texture. In: *Canadian Unconventional Resources Conference*. Society of Petroleum Engineers; 2011. https://doi.org/10.2118/147401-MS.
61 Davies J-P, Davies D-K. Stress-dependent permeability: characterization and modeling. In: *SPE Annual Technical Conference and Exhibition*. Society of Petroleum Engineers; 1999. https://doi.org/10.2118/56813-MS.
62 Barton N, Choubey V. The shear strength of rock joints in theory and practice. *Rock Mech*. 1977;10(1-2):1–54.
63 Lei Q. *Characterisation and Modelling of Natural Fracture Networks: Geometry, Geomechanics and Fluid Flow*. London: Imperial College London; 2016.
64 Olsson R, Barton N. An improved model for hydromechanical coupling during shearing of rock joints. *Int J Rock Mech Min Sci*. 2001;38(3):317–329.
65 Witherspoon PA, Wang JSY, Iwai K, Gale JE. Validity of cubic law for fluid flow in a deformable rock fracture. *Water Resour Res*. 1980;16(6):1016–1024.
66 Geuzaine C, Remacle J-F. Gmsh: a three-dimensional finite element mesh generator with built-in pre- and post-processing facilities. *Int J Numer Methods Eng*. 2009;79 (11):1309–1331.
67 *Tecplot. Tecplot 360 User's Manual*; 2014. http://www.tecplot.com.
68 Lie K-A. *An Introduction to Reservoir Simulation Using MATLAB: User Guide for the Matlab Reservoir Simulation Toolbox (MRST)*. Oslo, Norway: SINTEF ICT; 2016.
69 Gläser D, Helmig R, Flemisch B, Class H. A discrete fracture model for two-phase flow in fractured porous media. *Adv Water Resour*. 2017;110:335–348.
70 Karimi-Fard M, Durlofsky LJ, Aziz K. An efficient discrete-fracture model applicable for general-purpose reservoir simulators. *SPE J*. 2004;9(2):227–236.
71 Park K, Paulino GH. Computational implementation of the PPR potential-based cohesive model in ABAQUS: educational perspective. *Eng Fract Mech*. 2012;93: 239–262.
72 Ghosh G, Duddu R, Annavarapu C. A stabilized finite element method for enforcing stiff anisotropic cohesive laws using interface elements. *Comput Methods Appl Mech Eng*. 2019;348:1013–1038.
73 Yuan D, Peng L, Wu YS, Kang ZJ. Numerical simulation of multiphase flow in fractured vuggy porous medium using finite volume method. *Chin J Comput Mech*. 2013;30:144–149.
74 Comsol AB. *COMSOL Multiphysics User's Guide, Version 333*. Burlington, MA: COMSOL Inc; 2005.
75 Sargent RG. Verification and validation of simulation models. In: *Proceedings of the 2010 Winter Simulation Conference*. IEEE; 2010:166–183.